RAMAN AND BRILLOUIN SCATTERING

IN LiCAF AND LiSAF

CRYSTALS

By

CHARLES EDWARD HASTY

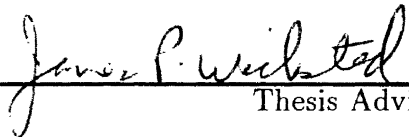Bachelor of Science

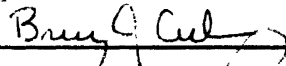Oklahoma State University

Stillwater, Oklahoma

1990

Submitted to the Faculty of the
Graduate College of the
Oklahoma State University
in partial fulfillment of
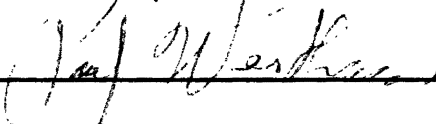the requirements for
the Degree of
MASTER OF SCIENCE
December, 1993

RAMAN AND BRILLOUIN SCATTERING
IN LiCAF AND LiSAF
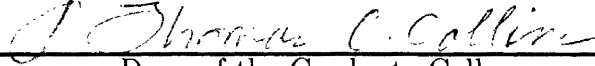## CRYSTALS

Thesis Approved:

_____
Thesis Adviser

_____

_____

_____
Dean of the Graduate College

ACKNOWLEDGMENTS

I wish to express my sincere thanks to the many people who have inspired and supported me through my college years. Although many lives have influenced mine, I could not do justice to their contributions in my life and this effort. I will keep these thanks relatively short and hope to not offend those I may have neglected to mention.

I would like to thank Dr. Bruce Ackerson, Dr. Paul Westhaus, and Dr. James Wicksted for their dedication to education and participation on my graduate committee. The faculty and staff of the Physics department I will always remember for the courteous, personable, and professional treatment received from their capable hands. Thanks are also due to my fellow members of the Wicksted research group. The Graduate School experience has been largely a good thing, and if any are responsible for this it would have to be the members of the group and my fellow graduate students.

My closest friends are responsible for any sanity I may have retained throughout my college experience. Elizabeth and Steve are undoubtedly some of the more patient people I know (they have to be, rest assured). Apollo and Karen have suffered many classes and my company for a long time, seemingly without damage. Many fishing excursions with Warren, although potentially hazardous to the welfare of others (and ourselves), have kept my peace of mind from completely disappearing. Of Chad, all that can be said is that he and I are so alike it is scary, and "We're not worthy!"

Finally, I would like to acknowledge my family; without their love and support, this endeavor would certainly have been less bearable, if not impossible. If I ever drew strength from somewhere, it would have to be from my mother Margaret, my father Wallace, and both my brothers Clark and Mark.

TABLE OF CONTENTS

LIST OF FIGURES

LIST OF TABLES

CHAPTER I

INTRODUCTION

Previous Studies

In a search for laser hosts providing a viable alternative to such powerhouses as Nd:YAG and Alexandrite, much effort has been dedicated to the investigation of fluoride compounds. Specifically, hosts are desired for the Chromium (Cr^{3+}) ion, since they result in four-level laser systems which provide laser output at relatively modest pumping energies. Another tendency of Chromium doped hosts is the existence of wide absorption bands, which allow for efficient energy transfer between a pumping source such as a flashlamp or another laser and the host.

The history of Chromium doped lasing materials began in 1974, and has (eventually) resulted in at least 15 different laser hosts, including Ti:Sapphire, Alexandrite, and Emerald lasers.[3] Of these, most are poor laser hosts due to either large scattering losses in the crystal or impurities within the crystal absorbing at the lasing wavelength. Another drawback associated with Chromium hosts is the difficulty with which they are grown. Most of these hosts are at least moderately difficult to grow, and in the case of Emerald, extremely hard to grow.

These fluoride hosts have several potential advantages over their oxide counterparts such as: low values of excited state absorption (ESA), negative dn/dt values (the important parameter for thermal lensing effects), resistance to ultraviolet solarization, broad absorption lineshapes, and potentially long fluorescence lifetimes for high energy storage. Unfortunately, they also encounter drawbacks such as: reduced mechanical strength, less resistance to very high temperatures due to lower melting points, high losses due to passive scattering within the crystal, and difficulty in crystal growth.

1

The crystals of interest within this study, LiCaAlF$_6$ (hereafter referred to as LiCAF) and LiSrAlF$_6$ (referred to as LiSAF), are named Colquiriite after the Bolivian tin mine in Colquiri where they were discovered. When doped with Chromium ions, these crystals become good laser hosts. Since LiCAF has the same structure as LiCaCrF$_6$, it is expected that the Chromium ions will be well suited to the LiCAF lattice. The first instance of these crystals' synthetic growth was by H. Newkirk at Lawrence Livermore National Laboratory in California in 1987. These crystals were very lossy, and much effort has gone into improving crystalline quality, since the scattering structures inside the crystal are definitely a detriment to laser operation.[2] Recently, a process of annealing these crystals and removing many of the defects was discovered, paving the way for good quality crystals to be supplied for laser applications.

Although there has been much interest in these crystals, studies of the Raman and Brillouin structures these crystal possess have not been attempted to our knowledge. Other properties have been extensively studied, such as: efficiency of LiCAF in various pumping arrangements, absorption and fluorescence studies, mechanical properties testing, and structure of scattering sites. These studies have shown that although the efficiency of both LiCAF and LiSAF hosts are high (near 80%), they have poor mechanical strength characteristics compared to Alexandrite. The fluorescence studies have proven that both hosts have wide absorption bands and therefore are well suited to flashlamp-pumped applications, as well as possessing a very broad tunability range (nearly 200 nm). The lifetime of the upper laser level in LiCAF is 175 μs, compared to 65 μs for LiSAF.[3,2] Other studies have shown that both the emission lifetime and the absorption lineshapes are relatively independent of Chromium content, allowing for the amount of chromium added to the host to be tailored to the individual application desired.[4] Overall, many applications should be well suited to these laser hosts, such as: spectroscopic excitation sources, range finders, and many others.

Work Reported in this Study

This study focuses upon the spectroscopic properties of the LiCAF host, and in the case of the Raman studies, this knowledge will be augmented with extra consideration of the properties of LiSAF. Both Raman and Brillouin studies of LiCAF are reported. Raman work was performed upon both LiCAF and LiSAF crystals, in some cases giving some insight into the types of atoms involved with particular normal mode vibrations. Any dependence of the Raman spectra upon Chromium doping is shown, although the results are not what was expected.

Brillouin scattering was performed only upon undoped LiCAF in an effort to determine the elastic and photoelastic constant values of the host lattice without interference due to Chromium doping. Four of the six elastic constants were determined; while all eight photoelastic constants were able to be experimentally investigated, seven of them were determined.

CHAPTER II

PHYSICAL PROPERTIES OF LiCAF AND LiSAF

Physical Data

Crystalline Structure

LiCAF, and its isomorph LiSAF, both possess a trigonal structure having the $\bar{3}m$ point group symmetry, which may also be denoted by D_{3d} . The LiCAF unit cell possesses 18 atoms in two units: $2(LiCaAlF_6)$, which are slightly offset with respect to one another, and having lattice constants of $a = 4.996 \; \overset{o}{A}$ and $c = 9.636 \; \overset{o}{A}$. This structure is illustrated in Figure 1. LiSAF structure is different from LiCAF in that Strontium is used in place of Calcium.[1]

When LiCAF is used as a laser host, it is doped with Chromium (Cr^{3+}) ions, which substitute for Aluminum in the crystal. Dopant concentration is usually in the neighborhood of 3% Cr^{3+} for both LiCAF and LiSAF, and this dopant produces a brilliant emerald green color.

Bulk Properties of LiCAF and LiSAF

In general, many of the important parameters needed for the analyses presented in this thesis are already known; pertinent others were measured by other experimenters in the earliest stages of this project. LiCAF, being a trigonal crystal, possesses two indices of refraction due to optical anisotropy. In the high symmetry crystalline direction (which will be referred to as the *extraordinary* index, denoted by n_e, and by convention this axis is called the $\hat{c}$ axis), the index of refraction is 1.3927, while in the *ordinary* direction it is 1.3940. Both of these values are interpolated for an excitation wavelength of 514.5 nm from a Sellmeier fit of the
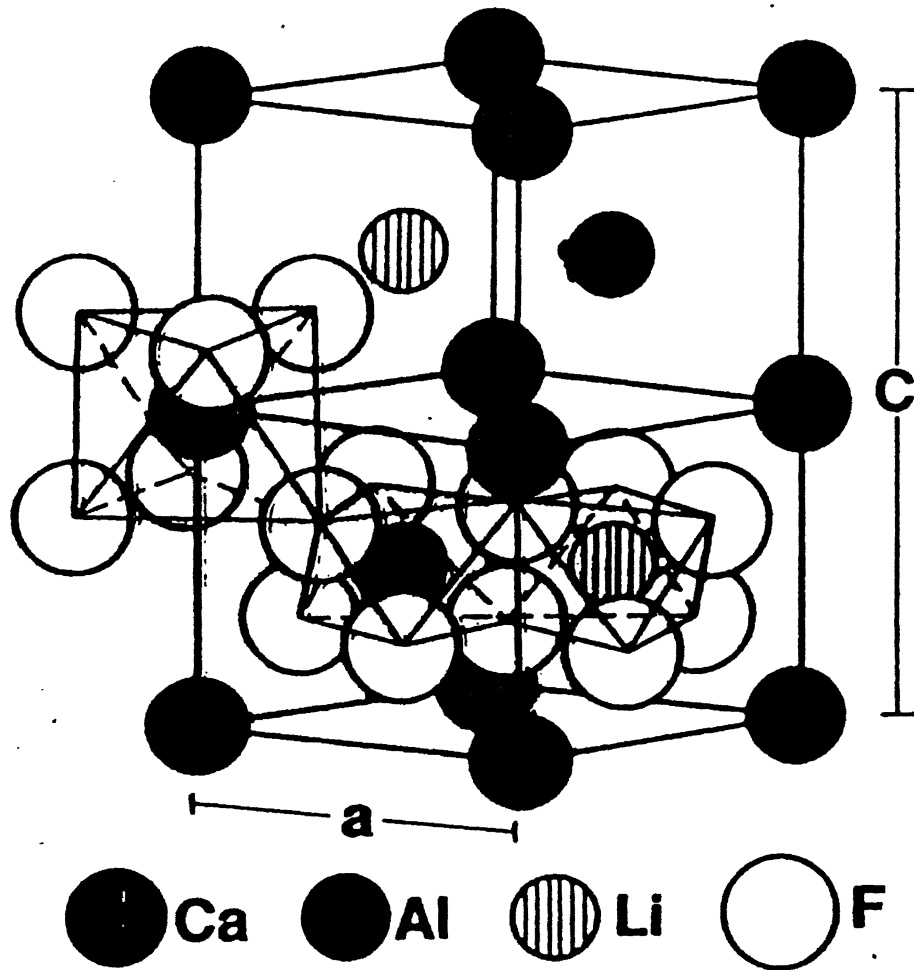
Figure 1. LiCAF unit cell

refractive index data performed by Payne and Chase.[2] The bulk density of the crystal, another important property in the elastic constant analysis, is found to be 2.95 $\frac{g}{cm^3}$.[3]

Absorption and Emission Spectra of LiCAF

The emission of absorption spectra for LiCAF crystals is illustrated in Figure 2. Attention should be given to the fact that the anisotropy gives rise to different spectra shapes for light propagating parallel and perpendicular to the $\hat{c}$ axis. For light parallel and perpendicular to $\hat{c}$, the peak absorption takes place around ~ 630 nm, while peak emission occurs near ~ 765 nm. The broad nature of the emission bands also indicate that the output of a LiCAF laser could be tuned over a wide range of values, from near 700 nm all the way out to around 900 nm.[1,4]

Group Theoretical Analysis

This section will explore the group theoretical determination of the number of Raman-active modes in LiCAF and how to see them experimentally. Most of this discussion is based upon the method of Colthup, Daly and Wiberly.[5]

Our analysis begins by calculation of the number of degrees of freedom of the unit cell:

$$\#DoF = 3 * N \tag{1}$$

where N is the number of atoms per unit cell, and the factor of 3 comes from the 3 dimensions that each atom may move in: $\hat{x}$, $\hat{y}$, and $\hat{z}$. Therefore, the number of degrees of freedom for all atoms in the unit cell is $3 * 18 = 54$. Recall that this number is also equivalent to the number of normal mode vibrations of the unit cell, and a convenient check on our results will use this fact. We will need the character table for LiCAF:

$$Symmetry\ Elements: I, 2S_6, 2C_3, S_2, 3C_2, 3\sigma_d$$
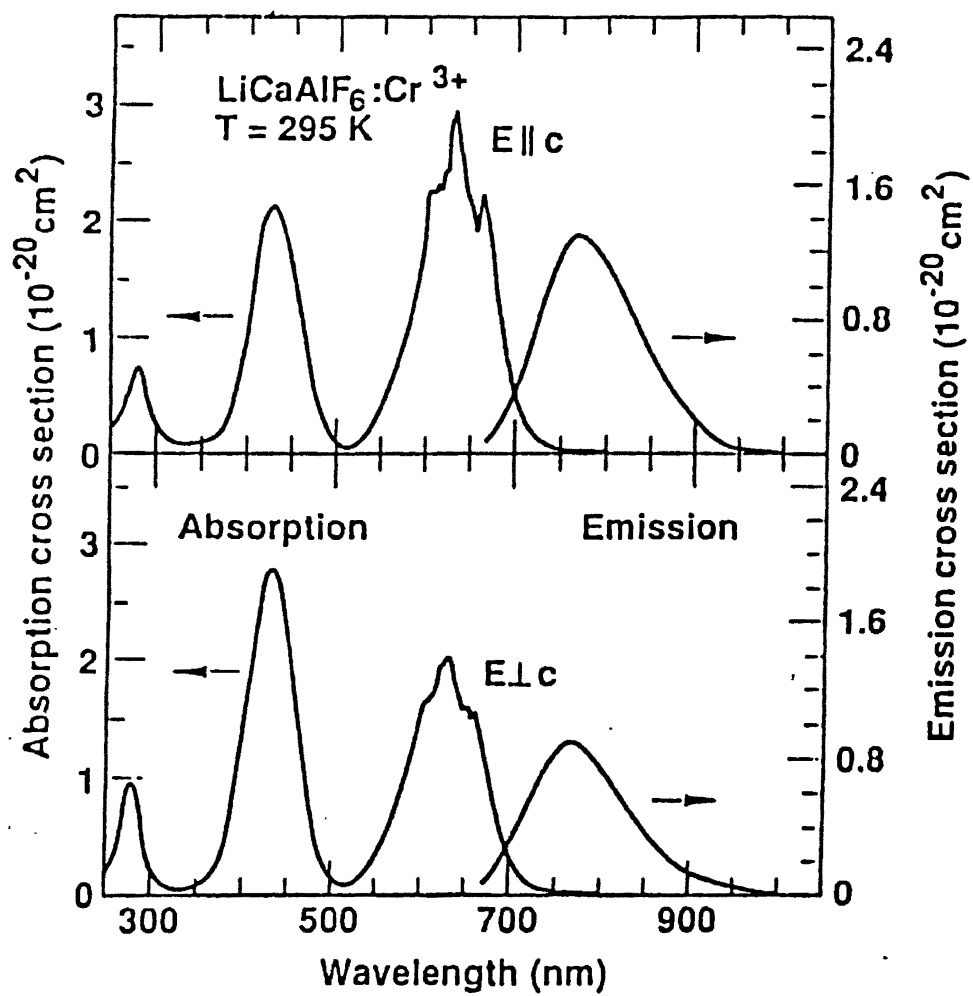
Figure 2. Absorption and Emission Spectra of LiCAF

D_{3d}	I	$2S_6$	$2C_3$	S_2	$3C_2$	$3\sigma_d$
A_{1g}	1	1	1	1	1	1
A_{1u}	1	-1	1	-1	1	-1
A_{2g}	1	1	1	1	-1	-1
A_{2u}	1	-1	1	-1	-1	1
E_g	2	-1	-1	2	0	0
E_u	2	1	-1	-2	0	0

Using group theory, the method for finding how many modes will show up in a spectrum for each type of atomic motion is given as:

$$N_i = \frac{1}{N_g} \sum_{\substack{all \\ classes}} N_e \chi(R)\chi_i(R) \tag{2}$$

where N_i is the number of times a type of mode appears, N_g is the total number of elements in the group, N_e is the number of elements in the eth class, $\chi(R)$ is the character of the atoms in the unit cell (which describes how their positions transform), and $\chi_i(R)$ is the character of the elements in the eth class for the ith mode. Given that the character table is known, we may calculate:

$$N_g = [1(I) + 2(S_6) + 2(C_3) + 1(S_2) + 3(C_3) + 3(\sigma_d)] = 12 \tag{3}$$

Care should be taken to distinguish the character of the group from the elements of the character table. The character $(\chi(R))$ of a material is defined as:

$$\chi(R) = U_R\chi = U_R(2\cos\varphi \pm 1) \tag{4}$$

for rotations, where the $\pm$ sign indicates a minus sign should be used for improper rotations, U_R is the number of atoms unchanged by the operation. and φ is the rotation angle. In general, the determination of the number of unchanged atoms could be quite difficult, and since our LiCAF crystal contains 18 atoms, we look for a shortcut. It turns out that for any atom whose position is unchanged, the site symmetry of that position will include the element of interest. For example:

looking up the site symmetry for the Li atoms, we find it is 32. Now, in order for this atom to retain its' position when undergoing say the C_3 operation, the site symmetry itself must contain the element operating upon it (i.e.- the symmetry of this site (32) must include the C_3 operation). If this is the case, then the number of atoms unchanged, in this case the 2 Li atoms, is 2. More on this shortly.

For the elements of symmetry possessed by LiCAF, the values of φ and χ are:

Symmetry Element :	I	$2S_6$	$2C_3$	S_2	$3C_2$	$3\sigma_d$
$\varphi =:$ (degrees)	0	60	120	180	180	0
χ	3	0	0	-3	-1	1

keeping in mind that improper rotations (S_i groups) warrant a minus sign and that the reflection plane is equivalent to an improper rotation through 0^0.

To determine the number of atoms unchanged by symmetry operations, we turn to the International Tables of Crystallography [16,5] for the site symmetries of each of the constituent species and their character tables, summarized below. The number within the table is the number of atoms whose positions are unchanged by the operation, while U_R is the sum of all atomic positions left unchanged by the operation.

Symmetry Element :	I	$2S_6$	$2C_3$	S_2	$3C_2$	$3\sigma_d$
$Li : 2$	2	0	2	0	2	0
$Ca : 2$	2	2	2	2	0	0
$Al : 2$	2	0	2	0	2	0
$F : 12$	12	0	0	0	0	0
$U_R :$	18	2	6	2	4	0

which implies the value of $\chi(R)$ (recalling that $\chi(R) = U_R\chi$):

$$\chi(R) = \quad 18\,(I)*3 \quad +2\,(S_6)*0 \quad +6\,(C_3)*0 \quad +2\,(S_2)*-3 \quad +4\,(C_2)*-1 \quad +0\,(\sigma_d)*1$$

thus we have:

$$\chi(R) = \quad 54\,(I) \quad +0\,(S_6) \quad +0\,(C_3) \quad +(-6)\,(S_2) \quad +(-4)\,(C_2) \quad +0\,(\sigma_d)$$

We now have all the information needed to determine which types of modes have what populations by using our relation for $N_i(R)$:

	I	S_6	C_3	S_2	C_2	σ_d	$T\!t\!l$
$A_{1g}:$	$\frac{1}{12}(1(54)1$	$+2(0)1$	$+2(0)1$	$+1(-6)1$	$+3(-4)1$	$+3(0)1) =$	3
$A_{1u}:$	$\frac{1}{12}(1(54)1$	$+2(0)-1$	$+2(0)1$	$+1(-6)-1$	$+3(-4)1$	$+3(0)-1) =$	1
$A_{2g}:$	$\frac{1}{12}(1(54)1$	$+2(0)1$	$+2(0)1$	$+1(-6)1$	$+3(-4)-1$	$+3(0)-1) =$	5
$A_{2u}:$	$\frac{1}{12}(1(54)1$	$+2(0)-1$	$+2(0)1$	$+1(-6)-1$	$+3(-4)-1$	$+3(0)1) =$	6
$E_g:$	$\frac{1}{12}(1(54)2$	$+2(0)-1$	$+2(0)-1$	$+1(-6)2$	$+3(-4)0$	$+3(0)0) =$	8
$E_u:$	$\frac{1}{12}(1(54)2$	$+2(0)1$	$+2(0)-1$	$+1(-6)-2$	$+3(-4)0$	$+3(0)0) =$	10

Therefore, we (finally) have the number of modes referenced to the kind of modes:

$$\Gamma_{ttl} = 3A_{1g} + 4A_{1u} + 5A_{2g} + 6A_{2u} + 8E_g + 10E_u \tag{5}$$

As advertised, we are now able to check our results with what we know: there are 54 modes (degrees of freedom), so given that the A modes are singly degenerate and the E modes are doubly degenerate, our relation should work out:

$$\Gamma_{ttl} = 3\,(1) + 4\,(1) + 5\,(1) + 6\,(1) + 8\,(2) + 10\,(2) = 54 \tag{6}$$

Keeping in mind that these are ALL the modes, both acoustic and optic, we find that the A_{2u} and one of the E_u modes are corresponding to net translations in the 3 fundamental directions, leaving us with 51 optic modes, both Raman and Infrared active:

$$\Gamma_{ttl} = 3\,(1) + 4\,(1) + 5\,(1) + 5\,(1) + 8\,(2) + 9\,(2) = 51 \tag{7}$$

One final piece of information which the character table relinquishes to us is the modes which are Raman active, and the polarizations of the scattered light necessary to see them experimentally. Thus we see that the 3 A_{1g} and 8 E_g modes are the only modes which are Raman active (the selection rules forbid the activity

of the A_{1u}, A_{2g}, A_{2u}, and E_u modes); moreover we have the number of them in each case.

It is also evident that the A_{1g} modes may be seen with a scattered polarization of [zz], while the E_g modes are seen with a scattered polarization of [y(x+z)].[16] Given the orientation of our sample, we choose to set up our experiments as follows: for the A_{1g} modes, we used a polarization scheme of x[zz]y; for the E_g modes, a scheme of x[y(x+z)]y was used. To explain the notation, the following convention is used:

$$P = k_i[\hat{e}_i\hat{e}_s]k_s \tag{8}$$

where the subscripts refer to incident and scattered, while the k terms are wavevector directions of the light and the $\hat{e}$ terms refer to electric field polarizations. As an illustration, when seeing the E_g modes, the incident light impinges upon the sample going in the $\hat{x}$ direction, is scattered in the $\hat{y}$ direction. The incident polarization was in the horizontal ($\hat{y}$) direction, and scrambled (non-polarized light) was collected from both the vertical and horizontal ($\hat{z}$ and $\hat{x}$) directions.[5,6]

CHAPTER III

RAMAN SPECTROSCOPY

Brief History of Raman Scattering

In 1923, Smekal predicted theoretically that the interaction between a material and an incident light beam could produce scattered light which differed in frequency from the incident beam. This theoretical prediction was verified by C.V. Raman investigating liquids in 1928 in India, and independently by Landsberg and Mendelstam studying quartz in Russia. The work performed by Raman lead directly to his Nobel Prize in 1930. Significant work on gases followed in 1929. These studies resulted in the polarizability theories of Placzek and Teller in 1933, which provided the basis for current theoretical models.

From the beginning, Raman scattering studies were difficult to perform because of equipment limitations. Raman scattering requires very intense radiation which also has a very narrow spectral linewidth, and this was difficult to obtain in the 1930 era. The most frequently used excitation source was a mercury lamp, with the spectral output passed through a series of filters to select the most intense lines. Spectral information was typically taken with spectrographs on photographic plates. Due to problems inherent in the excitation source, the use of this technique was not extremely widespread.

With the development of lasers the field enjoyed a resurgence of interest, due to the superior qualities of the laser as an excitation source, such as intensity, polarization, and narrow spectral linewidth. Photomultipliers of increasingly better quality were also used in conjunction with spectrometers to generate quantitative intensity data.[7]

Raman Scattering Theory

Whenever light is incident upon a sample, it may be reflected, transmitted, absorbed, or scattered. The light we will be interested in is scattered through interactions with a crystalline lattice, although the theory developed in this section is equally applicable to scattering events from gases, liquids, and solids. As we will see, light incident upon a crystalline lattice is scattered in a certain (non-random) manner which is very dependent upon the symmetry possessed by the lattice.

There are two different kinds of scattering of interest in this section: Rayleigh and Raman scattering. Rayleigh scattering is viewed as elastic scattering of a light photon from a molecule in the material upon which the beam is incident; thus the scattered photons have the same energy as the incident photons. Raman scattering is the inelastic scattering of a photon of light from a material, resulting in scattered photons which have energies *different* from incident photons. The Raman effect results in two processes: Stokes and Anti-Stokes scattering events. Stokes events result from incident light creating a phonon inside the material under study, and thus have less energy than incident photons. Anti-Stokes events result from incident photons scattering from phonons already present in the material, and have greater energies than incident photons. The terminology "Stokes" comes from Stokes' fluorescence rule: fluorescence always occurs at lower frequencies than that of the incident radiation.[5]

Note, however, that Raman processes are strictly distinct from fluorescence phenomena. Fluorescent transitions involve the absorption of photons of light (a transition to an excited electronic state) which are then re-radiated some $\sim 10^{-8}$ seconds later; whereas Raman processes involve no absorption or excited electronic states, and are typically completed within $\sim 10^{-12}$ seconds.[10] Although both Raman and Infrared active processes involve vibrational motions of the atoms, Raman scattering is distinct from Infrared spectroscopy, which is dependent upon absorption. These two scattering processes generally provide complementary information

about the material, and in crystals such as the ones we studied which have a center of symmetry, these two types of modes will be mutually exclusive to one another.

When light is scattered from a crystalline solid, it must conserve both its momentum and energy. For a Stokes scattering event:

$$\Delta\omega = \omega_i - \omega_s \tag{9}$$

and

$$\overrightarrow{q} = \overrightarrow{k_i} - \overrightarrow{k_s} \tag{10}$$

with ω indicating frequency, $\overrightarrow{q}$ the wavevector of the created phonon, $\overrightarrow{k}$ the wavevector of the photon, and subscripts i (incident) and s (scattered). Typical values for $\overrightarrow{k}$ are less than $\sim 3 \times 10^7$ m^{-1}, while the maximum wavevector for excitations within a crystal's Brillouin zone is $\sim 3 \times 10^{10}$ m^{-1}. This implies that the Raman shifts measure phonon frequencies at $\overrightarrow{q} \simeq 0$, since the amplitude of the phonon is relatively constant over an individual cell. If we now invoke the long wavelength approximation, which states that the value of the exciting field is essentially constant over many cells (which holds true since the wavelength of the excitation source is 514.5 nm and typical cell dimensions are 10 $\overset{\circ}{A}$ or less), and notice that the motions of the atoms are periodic in time, we see that any individual cells will experience the same perturbations. A major result of this line of reasoning is that now the analysis of the system may be reduced to an analysis of a single unit cell, which is representative of the entire crystal.[8]

In a 3 dimensional unit cell composed of n atoms, there are $3n$ *total degrees of freedom* for atomic motions. For all cellular systems, there are 4 types of independent (to a first-order approximation) cellular energies: translational, rotational, vibrational, and electronic transitional. These are listed in order from lowest energy to highest, and typically differ by at least an order of magnitude.[9] Of these energies, only rotational and vibrational energies contribute to Raman processes, and the net translation of all unit cells in any of the 3 principal directions of the system are ignored (since they lead directly to Brillouin scattering, which is discussed in Chapter 4). This reduces the total degrees of freedom of the system to

(3n-3). However, this is not to say that all normal modes will result in Raman modes.

These (3n-3) *internal degrees of freedom* of movement correspond to motions of the atoms called *normal modes of vibration*. Each of these (3n-3) independent normal modes may be characterized by a *normal coordinate*, denoted by Q_k, which varies periodically with the frequency of its' corresponding normal mode. It is important to note that each normal mode involves motions of the atoms which a) have the same frequency, b) require the atoms to pass through their equilibrium positions simultaneously, and c) are independent of other normal modes, since there may be situations where a single normal mode may be excited. While each normal mode may have a unique amplitude and frequency of vibration, the center of mass of the molecule does not translate, nor does the cell rotate.[5]

The analysis begins with a light beam from a monochromatic source (such as a laser) incident upon a sample, with the beam's electric field described by:

$$\vec{E} = \vec{E_0}\cos(\omega_i t) \tag{11}$$

with $\vec{E_0}$ describing the maximum intensity of the electric field, and ω_i the characteristic frequency of the laser beam. This incident field's oscillation perturbs the charge distribution of the material, giving rise to a dipole moment (which is generally expressed as the dipole moment per unit volume, or polarization) $\vec{P}$:

$$\vec{P} = \overleftrightarrow{\alpha}\vec{E} \tag{12}$$

with $\overleftrightarrow{\alpha}$ the polarizability tensor of the unit cell of the crystal. This polarizability tensor is symmetric and describes how the electronic charge distribution surrounding the atoms is altered by the oscillating electric field of the laser beam.

Note that this indicates that the induced dipole moments are oscillating and, as a consequence of Classical electromagnetic theory, are radiating light at their oscillation frequency. If the incident electric field affects the atoms in such a way as to induce small oscillations about their equilibrium positions, the polarizability

tensor may be expanded in a Taylor series about the equilibrium position:

$$\overleftrightarrow{\alpha} = \overleftrightarrow{\alpha_0} + \left[\sum_{j=1}^{3n-3} \left(\frac{\partial \overleftrightarrow{\alpha}}{\partial Q_j}\right)_{Q_j=0} Q_j\right] + \dots \tag{13}$$

where the derivatives are evaluated at the equilibrium positions, Q_j refers to the normal coordinates of the system, and the tensor $\overleftrightarrow{\alpha_0}$ is the equilibrium polarizability tensor. Recall that the normal coordinates are periodic, and may be written:

$$Q_k = Q_{k_0} \cos(\omega_k t) \tag{14}$$

with ω_k being the frequency of vibration of the kth normal mode. We now concentrate upon the (single) k^{th} normal mode. Taking a first-order approximation for the polarizability, substituting, and using a trigonometric identity, we find:

$$\overrightarrow{P} = \overleftrightarrow{\alpha_0}\overrightarrow{E_0}\cos(\omega_i t) + \left(\frac{\partial \overleftrightarrow{\alpha}}{\partial Q_k}\right)_0 \frac{Q_k \overrightarrow{E_0}}{2}\{\cos[(\omega_i - \omega_k)t] + \cos[(\omega_i + \omega_k)t]\} \tag{15}$$

Note that there are 3 cosine terms in the expansion: the first corresponds to *Rayleigh* scattering, the second and third terms to *Stokes* and *Anti-Stokes* scattering, respectively. Clearly, Rayleigh scattering takes place with the same frequency as the excitation source, Stokes scattering occurs at lower frequencies than that of the excitation source, and Anti-Stokes scattering at higher frequencies. Also note that the position of the Raman spectra is independent of the excitation frequency, as are the lineshapes of the Raman bands.[8,5,9,10]

It should also be noted that, for either Stokes or Anti-Stokes scattering to take place *at all*, there *must* be at least one $\left(\frac{\partial \overleftrightarrow{\alpha}}{\partial Q_k}\right) \neq 0$. These $\left(\frac{\partial \overleftrightarrow{\alpha}}{\partial Q_k}\right)$ represent distortions in the polarizability of the material, and are fundamentally what is responsible for the Raman scattering process, and are known as Raman selection rules.[10] Thus it may turn out that only a few of the many normal modes are Raman active. Another rule of thumb for determining if a mode is Raman active is the Mutual Exclusion Principle: for molecules or cells having a center of symmetry, vibrations which preserve the center of symmetry (called *gerade* modes) are not Infrared active; those vibrations which do not preserve the center (*ungerade* modes) are not Raman active.[9]

Although a Classical treatment of the problem obtains the fundamental results for Raman scattering correctly, it also predicts (incorrectly) that the intensities of the Stokes and Anti-Stokes components are equal. This is not the case, so a quantum mechanical argument must be used to predict these relative intensities. The correct ratio of the intensities is:

$$\frac{I_{Anti-Stokes}}{I_{Stokes}} = \left(\frac{\omega_i + \omega_k}{\omega_i - \omega_k}\right)^4 \exp\left[-\left(\frac{2\pi h \omega_k}{kT}\right)\right] \tag{16}$$

with h being Planck's constant, k Boltzmann's constant, and T the absolute temperature. The exponential term is due to the Boltzmann distribution of the atomic populations for a given vibrational mode.[5]

Raman Experimental Apparatus

All of the Raman data generated for both LiCAF and LiSAF crystals was taken with the following system setup, as detailed in Figure 3 . A Spectra-Physics model 2020 Argon-ion laser, operating at 514.5 nm, was used as the excitation source.

Since this source's output also included plasma lines as an undesirable side-effect, the laser beam was modified to remove these lines. First, the beam was expanded from approximately 3mm diameter to approximately 20~25 mm diameter, to help in the spatial dispersion caused by the next elements, a pair of Pellin-Broca prisms. These prisms guided the beam through a 30 cm focal length lens, and then through a 100 micron aperture placed at the lens' focal point. This aperture served as a spatial filter, removing the plasma lines, since the lines' different wavelengths resulted in differing dispersion through the Pellin-Broca system. Typical throughput of the aperture was ~90%. Beyond the aperture was a 10 cm focal length lens, serving to re-collimate the laser beam after passing through all the optics. Several reflections later, the beam passed through a polarization rotator, provided to insure the correct polarization of the beam at the sample.
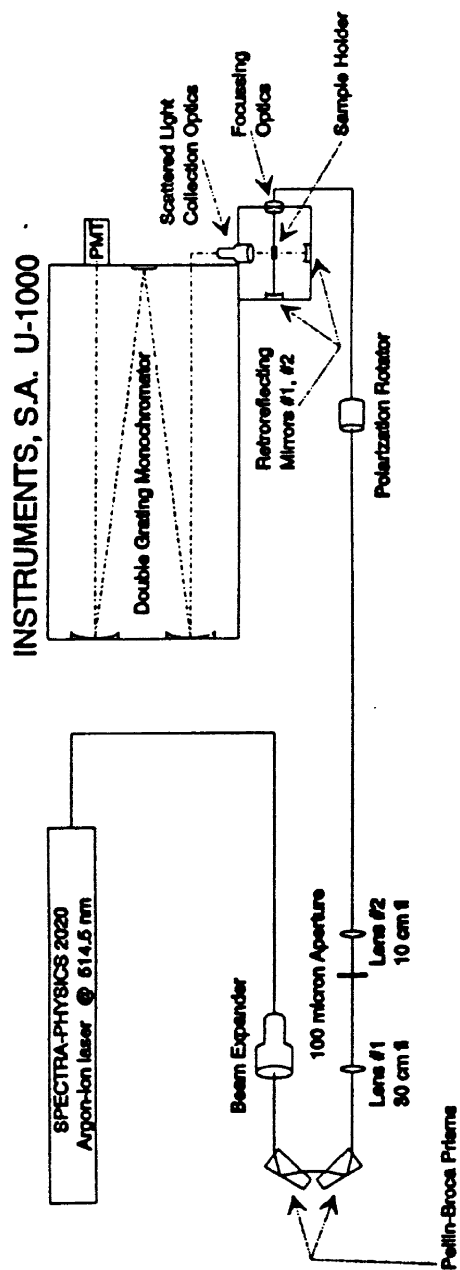
Figure 3. Experimental apparatus for Raman scattering.

After passing through focusing optics at the entrance to the sample chamber, the beam impinged upon the sample, propagated through the sample, and encountered a retro-reflecting mirror. This mirror returned the beam to the sample to increase the intensity in the scattering volume. Typical laser power at the sample was in the neighborhood of 100 mW; however, some scattering geometries required laser power of up to 750 mW at the sample. All scattering was performed at right angles to the incident beam, although this instrument also provides facilities for backscattering geometries.

The scattered light was collected and passed on to the Instruments, S. A. Ramanor U-1000 double grating monochromator. This monochromator was used with gratings ruled at 2400 lines per millimeter, and a focal length internal to the device of 1 meter. Typical resolutions attainable with this monochromator are near 0.5 cm^{-1} in the near UV and visible regions. This resolution, coupled with the stray light rejection of the instrument, imparts the ability to detect weak Raman signals near strong spectral lines. Light propagating through the system was detected with an RCA C3134A photomultiplier tube operated at 1800 volts. Since this photodetector produces a significant dark count at room temperatures, it was cooled with a thermo-electric cooling unit to about -25 degrees Celsius. Typical dark counts for this tube were reduced to around 10 to 30 counts per second.

The PMT signal was fed into a Spectra Link data acquisition system consisting of a pre-amplifier, discriminator, and a count ratemeter. Thus the data was supplied to an IBM XT personal computer, where all spectral data was taken with the Prism software package obtained from Instruments, S. A. and running under the Concurrent-Dos operating system. This software and hardware system provided control of most aspects of data acquisition and all manipulation and analysis of Raman spectral data.

Experimental Results and Data Analysis

All of the Raman data taken for the analysis performed in this thesis is shown Figures 4-7. The experimental configuration was essentially the same for all sets of data: all data was collected using a right angle scattering geometry, all scans used slits settings on the monochromator of 200 μm, all scans were taken over the range from 50 cm^{-1} to 650 cm^{-1} with a scan step size of 0.50 cm^{-1} and an integration time of 1 second. The polarizations of interest varied according to which set of modes were being studied, and the laser power incident upon the sample varied since some polarizations produced weaker scattering than others.

This study dealt with four different samples, each of which having the same crystalline orientation. Two samples of LiCAF were studied: LC3, which had no Chromium (Cr^{3+}) doping; and LC89, which was doped with 3% Cr^{3+} and was grown with an additional 3% of Lithium Fluoride (LiF) available to the crystal in the growth phase. An additional investigation of LiCAF was intended, with the inclusion of a 3% Cr^{3+} doped sample; however, due to sample unavailability this type of sample was never studied. Additionally, two samples of the crystalline isomorph of LiCAF called LiSAF were studied: LS91, grown with a very low concentration of Cr^{3+} dopant; and LS90, doped with 3% Cr^{3+}. Due to the nature of the LiSAF crystal, growth without a small percentage of Cr^{3+} is impossible. The sample LS91 is estimated to be doped with about 0.8% Cr^{3+}.

As has been shown in Chapter 2, the group theoretical calculations show that there are two types of normal modes which are Raman active (A_{1g} (3), E_g (8)) and the polarizations needed to view them (x[zz]y and x[y(z+x)]y, respectively). Table 1 shows the positions of the peaks of interest. Note that neither table includes those peaks which are unequivocally able to be associated with the other polarizations. Small misalignments in crystal orientation, incident beam polarization, and errors associated with the way the crystal has been cut may all result in these "ficticious" peaks, and are thus ignored.
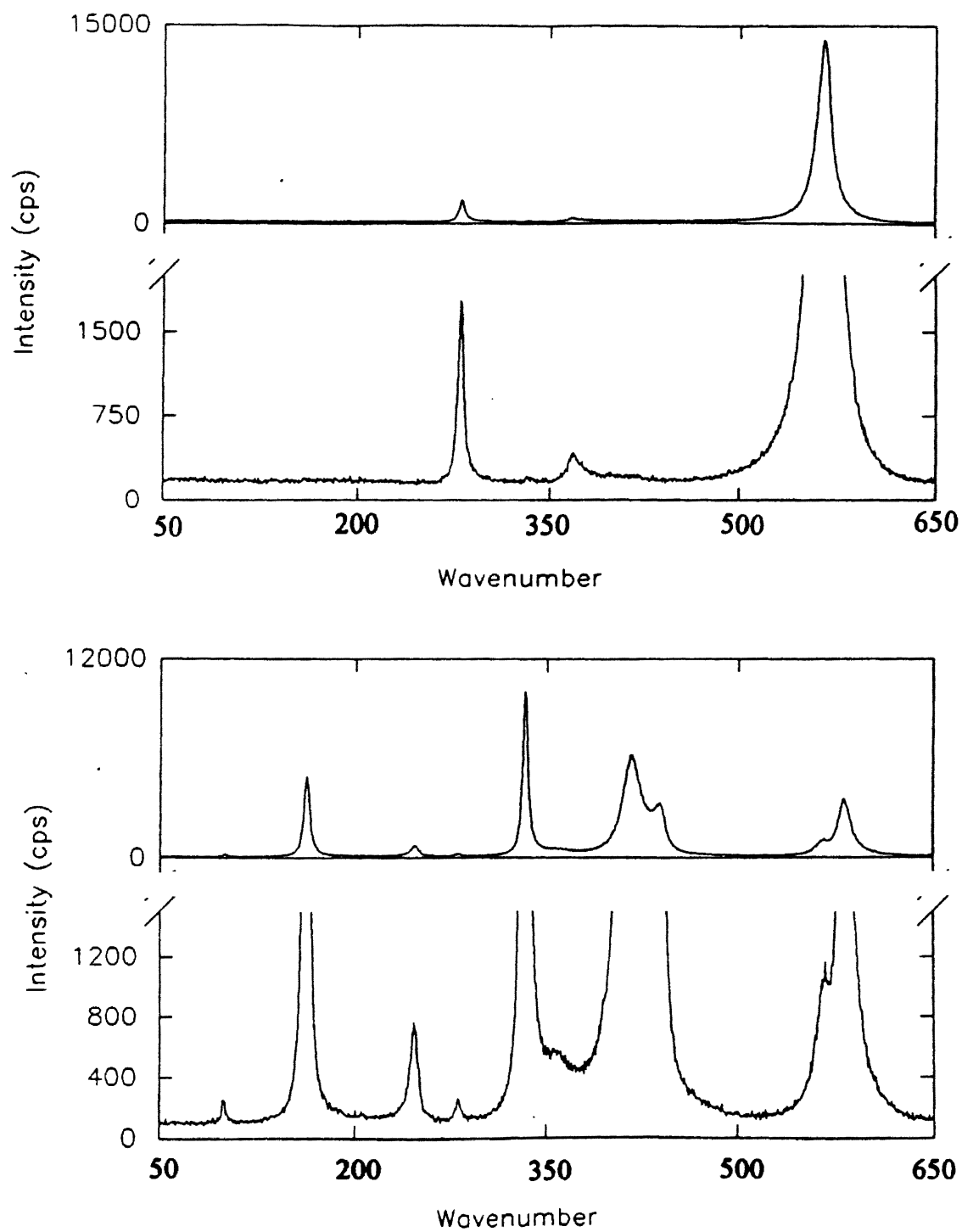
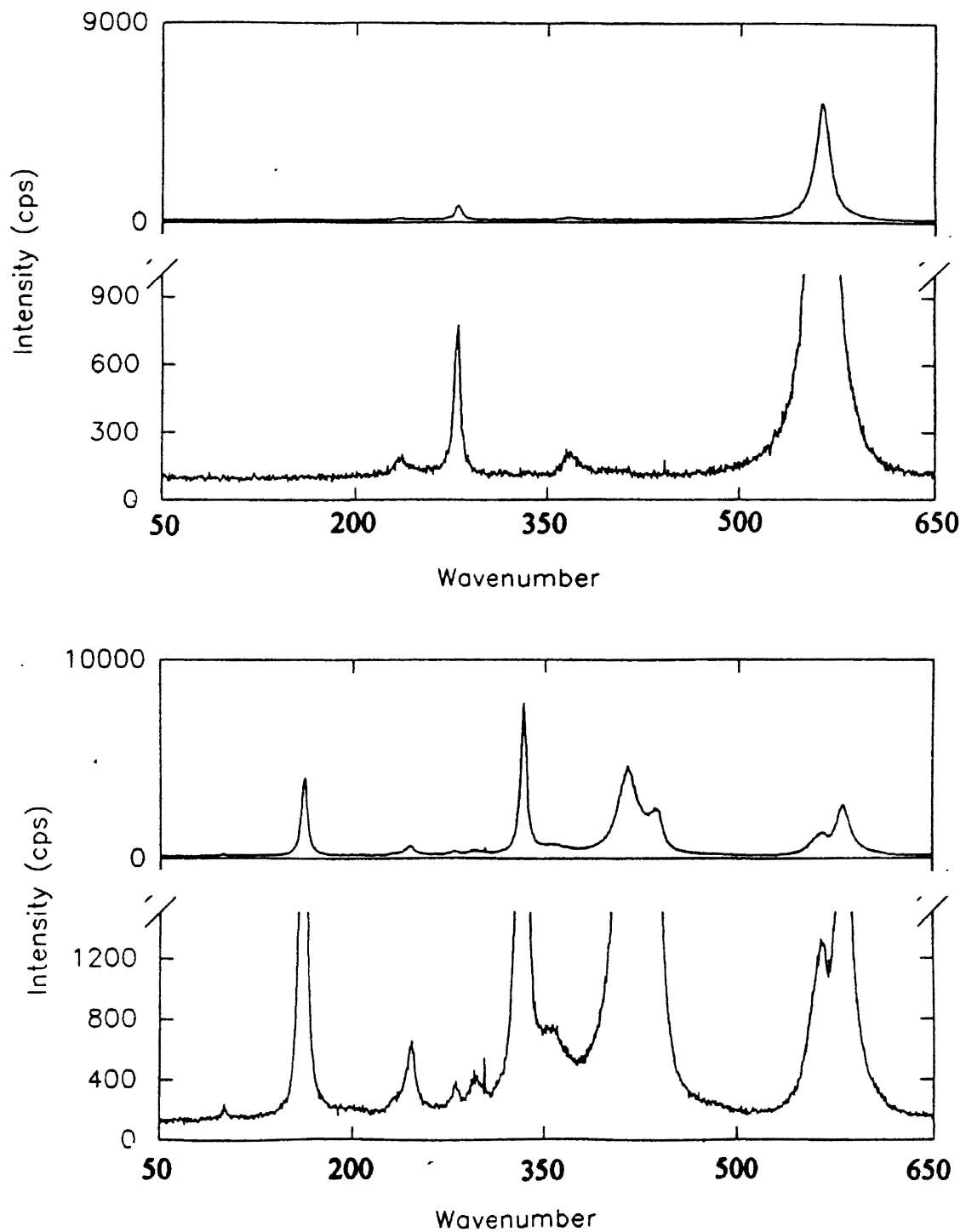Figure 4. Ag (top) and Eg (bottom) Modes in Undoped LiCAF.

Figure 5. Ag (top) and Eg (bottom) Modes in Cr Doped LiCAF.
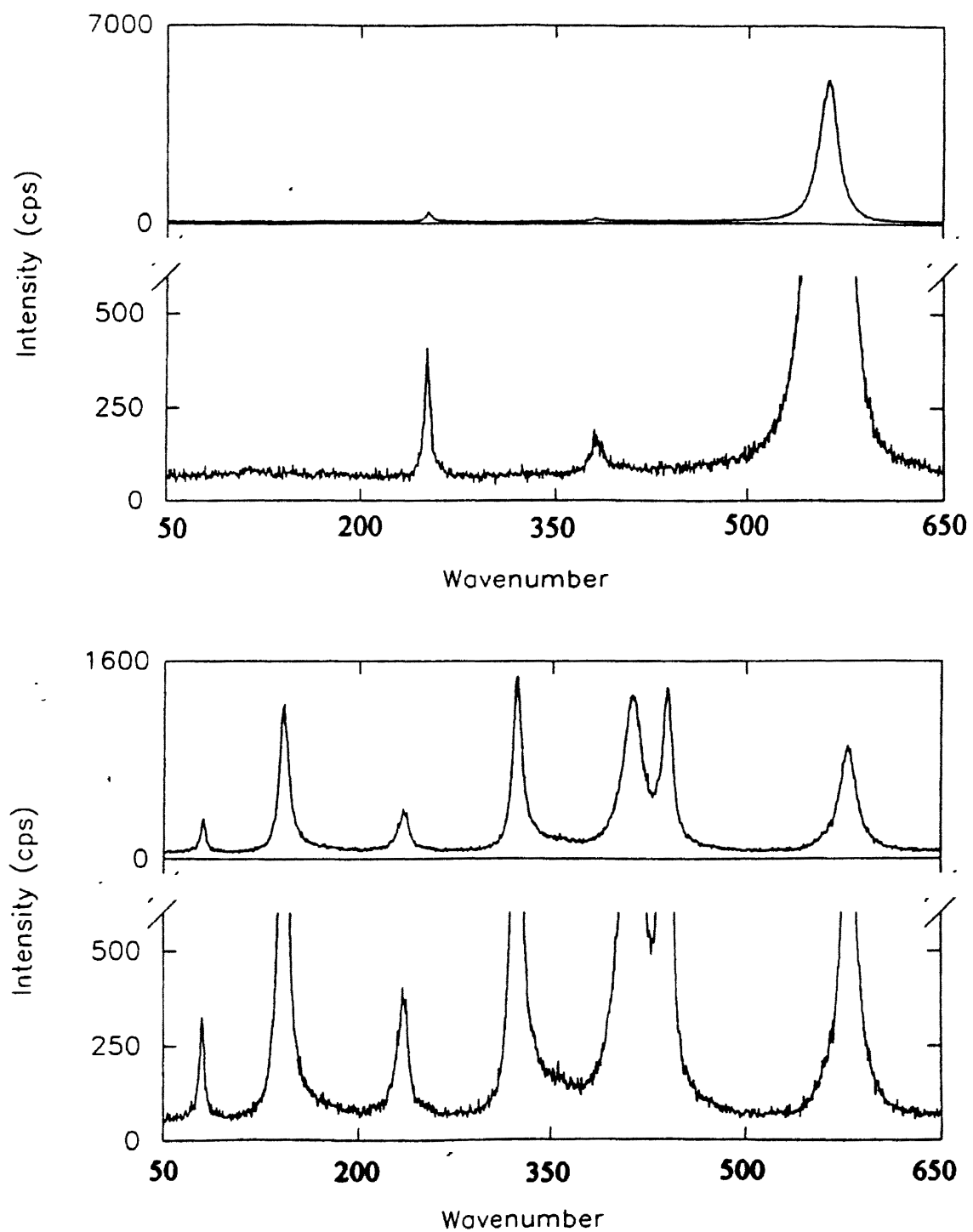
Figure 6. Ag (top) and Eg (bottom) Modes in Undoped LiSAF.
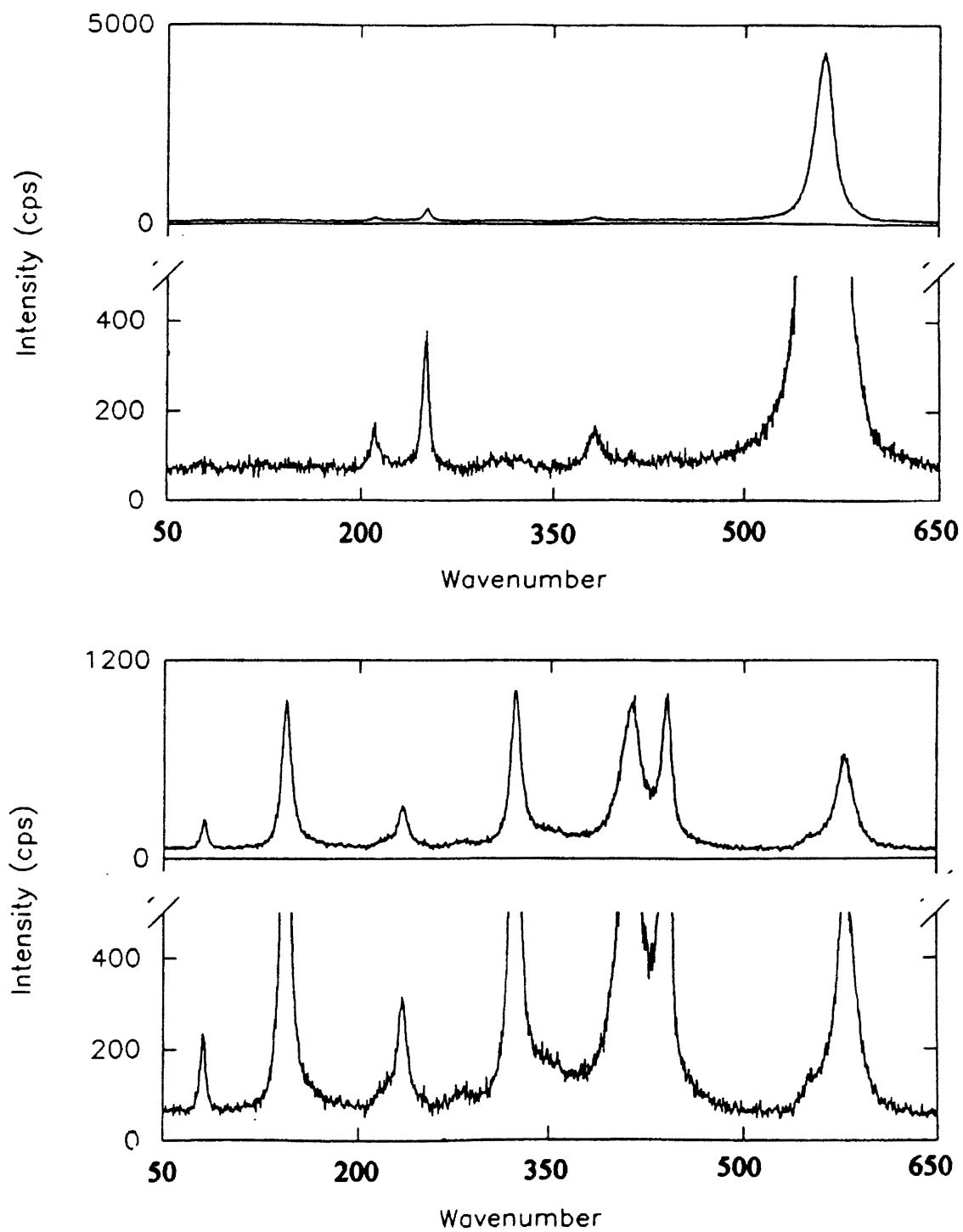
Figure 7. Ag (top) and Eg (bottom) Modes in Cr Doped LiSAF.

TABLES OF SPECTRAL DATA
FROM
LICAF AND LISAF CRYSTALS

A_{1g} modes: POLARIZATION [x(zz)y]

SAMPLE	LICAF	LICAF	LISAF	LISAF
FILENAME	LC3ZV	LC89ZV	LS90ZV	LS91ZV
DOPANT		3% Cr + LiF	Lo% Doped	3% Cr
		235		210
	281	281	251	251
	368	368	382	382
	565	565	561	561

E_g modes: POLARIZATION: [x(yx+yz)y]

SAMPLE	LICAF	LICAF	LISAF	LISAF
FILENAME	LC3YS	LC89YS	LS91YS	LS90YS
DOPANT		3% Cr + LiF	Lo% Doped	3% Cr
	99	99	80	80
	162	162	142	142
	246	246	233	233
		296		284
	333	333	322	322
	354	354	354?	354?
	414	414	410	410
	436	436	436	436
	581	581	576	576

Table I. Raman Modes in LiCAF and LiSAF.

A_{1g} Mode Analysis

In the undoped LiCAF sample (LC3), the most dominant mode is centered at 565 cm^{-1}, with the 281 cm^{-1} mode being the next most intense. When LiCAF is doped with 3% Cr^{3+} and is 3% LiF rich (LC89), the only occurrence of note is the appearance of a new A_{1g} mode at 235 cm^{-1}. This mode is NOT predicted by the group theoretical analysis, and is possibly due to Cr^{3+} or LiF occupying interstitial sites in the $\bar{3}m$ matrix. When low Cr^{3+} doped LiSAF (LS91) is studied, again three A_{1g} modes are detected, although their positions are shifted relative to undoped LiCAF. The most intense LiSAF mode is shifted to slightly lower energies by approximately 4 cm^{-1}, as is the next most intense mode which is now located at 251 cm^{-1}, a shift of 30 cm^{-1}. The remaining mode is shifted to higher energies by 14 cm^{-1}, to reside at 382 cm^{-1}. With the addition of 3% Cr^{3+} to LiSAF (LS90), the peak positions remain fixed except for the appearance of a new (again unpredicted) A_{1g} mode, which appears at 210 cm^{-1}. The other three modes A_{1g} modes are not shifted at all relative to the positions of the corresponding modes in the LS91 sample. When taken together, the appearance of the new (fourth) A_{1g} modes upon doping with 3% Cr^{3+} seems to imply that this mode is wholly due to the addition of Cr^{3+} ions and has no dependence upon the extra LiF present in the LC89 sample. Also note that in the undoped samples, there is a shift involved for *every* mode, thus the A_{1g} modes all involve motions of the Ca and Sr atoms.

E_g Mode Analysis

The E_g analysis is somewhat more complicated: the undoped LiCAF sample does indeed exhibit the 8 doubly degenerate E_g modes, although some explanation is required to verify this. Note that the correct polarization for seeing all 8 of the E_g modes is x[y(z+x)]y, and that this spectra actually consists of contributions from vertical (yz) and horizontal (yx) polarizations. There are 7 easily observable modes (not including, of course, the A_{1g} modes visible at 281 cm^{-1} and 565 cm^{-1}): 99, 162, 246, 333, 414, 436, and 581 cm^{-1}. By examining the spectra in the region

centered about 360 cm^{-1}, it was noted that there appears to be a hint of further structure between the modes at 333 and 414 cm^{-1}. When the vertically- and horizontally-polarized data were taken, it became apparent that there was indeed a weak Raman mode centered at $\sim$354 cm^{-1}. Thus the missing eighth mode was found.

Study of the 3% Cr^{3+} and 3% LiF rich doped LiCAF (LC89) resulted in the exact same spectra, with the addition of a new E_g mode at 296 cm^{-1}. Again it is not clear why this mode is present, other than the possibility that the Cr^{3+} ions may be occupying normally unavailable positions within the crystal lattice. Low percentage Cr^{3+} doped LiSAF (LS91) has 8 E_g modes, all of which are analogous to the modes of undoped LiCAF and most of which are shifted to lower energies by 4 to 20 cm^{-1}. An interesting feature of this spectra is that, relative to undoped LiCAF, the relative intensities of some of the modes have changed. The first mode at 80 cm^{-1} has become much stronger, as has the third mode at 233 cm^{-1}, and the 436 cm^{-1} mode has attained an intensity nearly equal to its' neighbor mode at 410 cm^{-1}. When LiSAF is doped with 3% Cr^{3+} (LS90), a new (ninth) mode appears at 284 cm^{-1}. This is the only change in the spectra relative to that of undoped LiSAF. One final point: note that for the E_g modes at 354 cm^{-1} and 436 cm^{-1}, there is no shift at all in any scan relative to undoped LiCAF. This indicates that these modes are independent of the Ca and Sr motions and Cr^{3+} doping.

CHAPTER IV

BRILLOUIN SPECTROSCOPY

Brief History of Brillouin Scattering

Brillouin scattering was first predicted theoretically by L. Brillouin in 1922, but remained unverified until the work of Gross on liquids and solids in 1930.[11] All early measurements were hampered by the state of equipment technology, since typical Brillouin shifts are 1 cm^{-1} or less. The equipment of the period was simply not accurate enough to allow clear observations, much less in-depth studies. Excitation sources of the period were typically mercury-discharge lamps, and the detectors used were spectrographs; all but the best lacked sufficiently high resolution to see the Brillouin structures.

The first confirmation of the theory resulted from investigations into Raman shifts very close to the excitation line by Gross, and later by Meyer and Ramm, Birus, and Rafalowski. However, none of these experimentalists had photographic evidence of the effect, and this was the case until the work of Rao in 1934. Rao used a special mercury lamp and Fabry-Perot system to study liquids, and is credited as the first observer with solid (photographic) evidence of this effect.[?] Much work was performed, but in 1952 the limit of experimental equipment to verify theoretical predictions had been reached.

When the laser was developed, interest in the field blossomed, since now experimenters had the high intensity, narrow bandwidth excitation source needed for high precision measurements.[11] The first use of lasers to study the Brillouin effect was reported by Chiao, et al in 1964; others soon became active in the field.[12] Since these studies, Brillouin spectroscopy has become a very widespread

tool for investigation of material properties, the most important of which are elastic and photoelastic constants.

Brillouin Theory

As was seen in Chapter 2, light incident upon a crystal perturbs the polarizability of the crystal, inciting scattered light of a different frequency than that of the excitation source. This scattered light essentially results from two types of atomic motions inside the crystal: motions in which the atoms move *out of phase* in such a way as to keep the center of mass of the unit cell from moving, and those *in phase* motions which result in a net change in the position of the center of mass of the unit cell. The former motions, by far the most numerous, are called *optic modes*, lead directly to Raman scattering processes. The latter are called *acoustic modes* since their net effect is to propagate a density wave through the crystal, and in the case of no degeneracies, number exactly three.[13]

These acoustic modes are responsible for a different type of light scattering, in which this sound or density wave perturbs the index of refraction and in effect scatters the incident light off of a moving diffraction grating. Thus the scattered light is Doppler shifted to both higher and lower frequencies than the incident beam. Now, assuming that these thermally induced sound waves (phonons) in the crystal set up a well defined diffraction grating,

$$\lambda_{m_i} = \frac{\lambda_0}{n_{m_i}} = 2\lambda_0 \sin(\frac{\theta}{2}) \tag{17}$$

where λ_{m_i} and n_{m_i} are the wavelength of light inside the media and the index of refraction for that media in the ith direction, λ_0 is the wavelength of the light in free space, and θ is the angle between the incident and scattered light (scattering angle). Recall that the grating is moving with velocity V (sound velocity), and the resulting doppler shift is:

$$\Delta\omega_{Brillouin_i} = \Delta\omega_{B_i} = \pm 2V_{s_i} n_{m_i}\omega_0 \sin(\frac{\theta}{2}) \tag{18}$$

with V_{s_i} the velocity of the sound wave in the ith direction, and ω_0 the angular frequency of the excitation source. This is the equation derived by Brillouin,

verifying that sound waves do indeed distort the incident beam.[8,?] Also be aware that, in general, this equation predicts 3 distinct values for the Brillouin shifts. This is not to say, however, that there may not be degenerate shifts.

The question now is: knowing the distortions occur, how can one relate the distortions to intrinsic properties of the material? The answer lies in a complicated series of manipulations, and they will only be surveyed here. For a more complete treatment, the reader is referred to Cummins and Shoen. [14]

To begin the analysis, we consider an elastic medium which has density ρ, displacements from atomic equilibrium positions denoted by u_i (the index i indicating the x_i^{th} Cartesian axis), and we assume that the harmonic approximation holds for the interaction between nearest neighbors. Considering the equations of atomic motion for the system, concentrating only on the ith atomic direction:

$$\rho \, \ddot{u}_i = \sum_{j,k,l=1}^{3} \frac{\partial^2 u_k}{\partial x_j \partial x_l} \tag{19}$$

Now, assuming plane wave solutions to this equation of the form:

$$u_i = u_{i_0} \exp[i(\overrightarrow{q} \cdot \overrightarrow{R} - \omega t)] \tag{20}$$

with the long wavelength approximation (the wavelength of excitation is much larger than the interatomic spacing, implying that ω is linear in q):

$$\omega = vq \tag{21}$$

where v is the velocity of sound, it can be shown that:

$$\sum_{j,k,l=1}^{3} \left[C_{ijkl} \widehat{q}_j \widehat{q}_l - \rho v^2 \delta_{ik} \right] u_{k_0} = 0 \tag{22}$$

where $\widehat{q}_j$ is the direction cosine of $\overrightarrow{q}$ in the jth direction and δ_{il} is a Dirac delta function. This has nonzero solutions only if the determinant vanishes:

$$\left| C_{ijkl} \widehat{q}_j \widehat{q}_k - \rho v^2 \delta_{il} \right| = 0 \tag{23}$$

(summation is implied). Choosing the ith direction, this equation results in a series of 3 equations:

$$\begin{vmatrix} \lambda_{11} - \rho v_i^2 & \lambda_{12} & \lambda_{13} \\ \lambda_{12} & \lambda_{22} - \rho v_i^2 & \lambda_{23} \\ \lambda_{13} & \lambda_{23} & \lambda_{33} - \rho v_i^2 \end{vmatrix} = 0 \tag{24}$$

with

$$\lambda_{11} = \hat{q}_x^2 C_{11} + \hat{q}_y^2 C_{66} + \hat{q}_z^2 C_{55} + 2\hat{q}_y\hat{q}_z C_{56} + 2\hat{q}_x\hat{q}_z C_{15} + 2\hat{q}_x\hat{q}_y C_{16} \tag{25}$$

$$\lambda_{22} = \hat{q}_x^2 C_{66} + \hat{q}_y^2 C_{22} + \hat{q}_z^2 C_{44} + 2\hat{q}_y\hat{q}_z C_{24} + 2\hat{q}_x\hat{q}_z C_{46} + 2\hat{q}_x\hat{q}_y C_{26} \tag{26}$$

$$\lambda_{33} = \hat{q}_x^2 C_{55} + \hat{q}_y^2 C_{44} + \hat{q}_z^2 C_{33} + 2\hat{q}_y\hat{q}_z C_{34} + 2\hat{q}_x\hat{q}_z C_{35} + 2\hat{q}_x\hat{q}_y C_{45} \tag{27}$$

$$\lambda_{12} = \hat{q}_x^2 C_{16} + \hat{q}_y^2 C_{26} + \hat{q}_z^2 C_{45} + \hat{q}_y\hat{q}_z(C_{46}+C_{25}) + \hat{q}_x\hat{q}_z(C_{14}+C_{56}) + \hat{q}_x\hat{q}_y(C_{12}+C_{66}) \tag{28}$$

$$\lambda_{13} = \hat{q}_x^2 C_{15} + \hat{q}_y^2 C_{46} + \hat{q}_z^2 C_{35} + \hat{q}_y\hat{q}_z(C_{45}+C_{36}) + \hat{q}_x\hat{q}_z(C_{13}+C_{55}) + \hat{q}_x\hat{q}_y(C_{14}+C_{56}) \tag{29}$$

$$\lambda_{23} = \hat{q}_x^2 C_{56} + \hat{q}_y^2 C_{24} + \hat{q}_z^2 C_{34} + \hat{q}_y\hat{q}_z(C_{44}+C_{23}) + \hat{q}_x\hat{q}_z(C_{36}+C_{45}) + \hat{q}_x\hat{q}_y(C_{25}+C_{46}) \tag{30}$$

Note that the notation has changed.[8,14] This is because the previous discussion had at its' roots (and not really discussed) the material's stress tensor (σ_{ij}) and the strain tensor (ϵ_{kl}), which are related to the elastic stiffness tensor.

While σ_{ij} and ϵ_{kl} are second rank tensors (each of which has 9 independent elements), C_{ijkl} is a fourth rank tensor having up to 81 independent elements. Both the stress and strain tensors are symmetric and it can be shown that this symmetry leads to a reduction in the number of independent terms in the elastic stiffness tensor if six-component notation is used.[15]

Using this convention has the advantage of reducing the number of independent elastic stiffness constants from 81 to 36. This (new) elastic stiffness tensor is also symmetric, further reducing the number of constants to 21. Crystalline symmetry, given any crystal type other than mono- or triclinic, will significantly reduce this number of constants even further.[15] For instance, LiCAF crystals have the symmetry of the $\bar{3}m$ point group, and thus the elastic stiffness tensor has

exactly 6 independent constants. Incidentally, most of the discussion from here on out will rely primarily upon the 6-component notation.

Given the velocity of propagation of the sound wave in a crystalline direction, information about the elastic constants is now available by solving this system of equations:

$$(\lambda_{11} - \rho v^2)u_x + \lambda_{12}u_y + \lambda_{13}u_z = 0 \tag{31}$$

$$\lambda_{12}u_x + (\lambda_{22} - \rho v^2)u_y + \lambda_{23}u_z = 0 \tag{32}$$

$$\lambda_{13}u_x + \lambda_{23}u_y + (\lambda_{33} - \rho v^2)u_z = 0 \tag{33}$$

Of course, one may turn the argument around and predict the velocity of the sound wave given the elastic constants. However, this is not all of the information able to be gained from the crystal. Given other basic information about the crystal, such as dielectric constant values, the photoelastic or Pockels coefficients may be evaluated.

The Rayleigh ratio, or differential cross section per unit volume, will relate the method by which researchers may select spectra due to a particular photoelastic constant, and also derive its' numerical value. The Rayleigh ratio is given by:

$$R^j = \frac{kT\omega_s^4}{32\pi^2 c^4 \rho v_j^2} \left[\hat{e}_s \cdot \overleftrightarrow{T^i} \cdot \hat{e}_0\right]^2 \left(\frac{n_s}{n_0}\right) \tag{34}$$

where T is the absolute temperature, ω_s the frequency of the scattered light, $\overleftrightarrow{T^i}$ the Brillouin tensor for the ith direction, and $\hat{e}_s$ and $\hat{e}_0$ the directions of the scattered and incident light, respectively. The factor $\left[\hat{e}_s \cdot \overleftrightarrow{T^i} \cdot \hat{e}_0\right]$ allows one to determine what photoelastic constants are actually contributing to the spectra under study. There exists another way of thinking about the Rayleigh ratio, involving the integrated intensities from both a standard sample and the crystal of interest. Since the Brillouin signal intensity is proportional to the Rayleigh ratio (scattering cross-section), it can be shown that[?]:

$$\frac{I_{sample}}{I_{std}} = \left(\frac{R_{sample}}{R_{std}}\right) \left(\frac{f_{sample}}{f_{std}}\right) \tag{35}$$

where the I's refer to integrated intensities, and the f's are correction factors due to both transmission through the sample and solid angle corrections. The values of f are given by:

$$f = \frac{16 n_i}{n_s \left(n_i + 1\right)^2 \left(n_s + 1\right)^2} \qquad (36)$$

Now, recalling that the velocity of the phonon can be expressed in terms of the Brillouin shift in cm^{-1}:

$$v = \frac{\lambda_0 c \Delta\omega_{Br}}{2n \sin\left(\frac{\theta}{2}\right)} \qquad (37)$$

we may arrive (after much manipulation of 34,35,36, and 37) at the following expression relating the sample's constants to the standard's spectra:

$$\left[\widehat{e}_s \cdot \overleftrightarrow{T^i} \cdot \widehat{e}_0\right]_{sample} = \left(\frac{\rho I}{\rho_{std} I_{std}}\right)^{\frac{1}{2}} \left[\frac{\left(n_i + 1\right)\left(n_s + 1\right)}{\left(n_i + 1\right)^2_{std}}\right] \left(\frac{n_{std}}{n}\right) \left(\frac{\Delta\omega_{Br}}{\Delta\omega_{Br_{std}}}\right) \left[\widehat{e}_s \cdot \overleftrightarrow{T^i} \cdot \widehat{e}_0\right]_{std} \qquad (38)$$

Note that for LiCAF, the values of the ordinary and extraordinary indices of refraction are $n_i = 1.3940$, and $n_e = 1.3927$; the average of which is $\overline{n} = 1.3934$. This average value of the refractive indices will be used to simplify the expression to:

$$\left[\widehat{e}_s \cdot \overleftrightarrow{T^i} \cdot \widehat{e}_0\right]_{sample} = \left(\frac{\rho I}{\rho_{std} I_{std}}\right)^{\frac{1}{2}} \left[\frac{\left(\overline{n} + 1\right)^2}{\left(n_i + 1\right)^2_{std}}\right] \left(\frac{n_{std}}{\overline{n}}\right) \left(\frac{\Delta\omega_{Br}}{\Delta\omega_{Br_{std}}}\right) \left[\widehat{e}_s \cdot \overleftrightarrow{T^i} \cdot \widehat{e}_0\right]_{std} \qquad (39)$$

This relationship allows one to determine the values of the (possible) combination of photoelastic constants for any individual sample.

In order to find out which photoelastic constants will be seen under experimental conditions, knowledge of the Brillouin tensors for the correct scattering geometry and crystalline orientation is a must. An extensive collection of Brillouin tensors for many point groups are available in Cummins and Shoen [14], as is a method of generating tensors not supplied in that source. Knowing the orientations relative to the crystal under study of the incident and scattered directions and polarizations allows a table to be made which will serve as a valuable

reference when determining which experimental configuration to use. A more detailed explanation and further examples are supplied in the data analysis section following.

Brillouin Experimental Apparatus

The experimental setup under which all Brillouin data discussed in this chapter was taken is detailed in Figure 8 . A Spectra-Physics model 2020 Argon-Ion laser, with its output modulated by an air-spaced etalon for the 514.5 nm line, was used as the excitation source. The intracavity etalon served to narrow the output bandwidth of the laser to about 5 Mhz, and allowed single-mode output powers up to around 750 mW. This output beam passed through a polarizer and was then focused into the sample with a 20 cm focal length lens.

The scattering geometry used was at 90 degrees to the incident beam, and scattered light from the sample was collected using an Olympus 55 mm focal length camera lens. This light was then passed through a 100 micron aperture (which was used as the point source of light for the remainder of the optics) and recollimated using another Olympus camera lens which had a focal length of 50 mm, followed with another polarizer.

Polarized scattered light then entered into the Burleigh Instruments RC-110 Fabry-Perot interferometer, which consists of a pair of extremely well polished mirrors (polished to $\lambda/200$ for 514.5 nm light) wedded to a series of piezoelectric stacks which allow the intracavity spacing of the device to be changed with high precision. While the instrument is capable of single-, triple-, and quintuple-pass operation, all experiments were performed in triple-pass mode. Typical finesse for Brillouin data collected for this thesis was from the upper forties to mid fifties.

All light from the Fabry-Perot system was then passed through a neutral density filter (to decrease the total intensity at the photodetector), focused through an aperture, and refocused onto the photocathode of the ITT FW-130 photomultiplier tube. Thermoelectrically cooled to approximately -25 degrees Celsius, this high sensitivity tube characteristically produced dark counts of 1 to 2 counts per second.
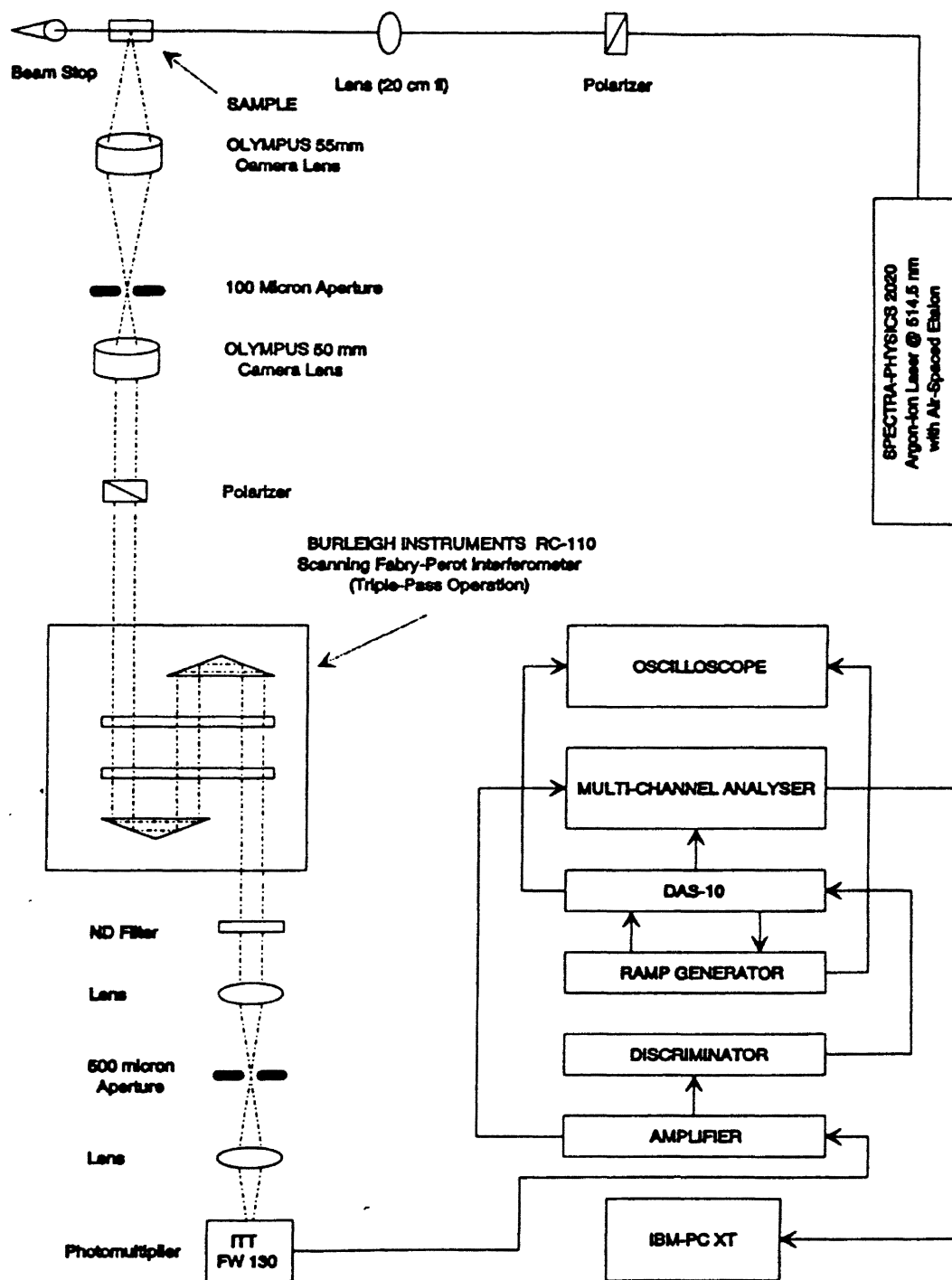
Figure 8. Experimental apparatus for Brillouin scattering

Output from this tube was passed to a Canberra Model 814 combination pream-plifier/amplifier/discriminator (PAD), which provided a signal to both the DAS-10 Fabry-Perot stabilization system and the Canberra multi-channel analyzer.

Control and stabilization of the Fabry-Perot was accomplished using two devices: the DAS-10 stabilization system and the Ramp Generator, both of which are produced by Burleigh Instruments. The Ramp Generator allowed different ramp times and ramp voltages. By altering the ramp voltage, different numbers of Rayleigh orders could be positioned under the ramp sent to the Fabry-Perot. Typically three or four Rayleigh orders were positioned under the ramp when data was collected, the scans were all performed using a ramp duration of 500 milliseconds, and a total of 10,000 sweeps of the Fabry-Perot were collected. The DAS-10 system corrected the response of the Fabry-Perot to insure its' long-term stability. For alignment purposes, output from both the Ramp Generator and the DAS-10 was sent to an oscilloscope.

Data collection was achieved through the use of a Canberra Series 35+ multi-channel analyzer, triggered by the DAS-10 to collect data from the PAD. Up to four sets of data (consisting of 1024 channels per set) could be stored and manipulated in the memory of the Canberra, and data could also be downloaded into an IBM PC-XT computer.

Experimental Results and Data Analysis

The Brillouin data taken in this study was all taken under nearly the same experimental conditions. The only exception is the laser intensity, which varied from $\sim$ 50 mW to around 500 mW, as a result of low scattering intensity. All scans on the Fabry-Perot system were performed at a sweep time of 500 milliseconds, and the free spectral range of the system was set to provide at least 3 Rayleigh orders under the ramp. Typical values of the free spectral range were $\sim 2\ cm^{-1}$.

Only two samples of LiCAF were available for this study, and this technique was not performed upon LiSAF crystals at all. The two LiCAF crystals were previously returned to Lawrence Livermore Labs for an annealing process, which

reduced the scattering losses in them by approximately an order of magnitude. Both crystals were undoped LiCAF, and had a volume of roughly 1 cm^3. The first was cut with the $\hat{y}$ and $\hat{z}$ axes along the diagonals of a square cross-section, with the $\hat{x}$ axis perpendicular to the third crystal face. This allows investigation of the $\hat{y}$ and $\hat{z}$ phonons. The second crystal was cut with the $\hat{x}$ and $\hat{y}$ axes perpendicular to the faces of a square cross-section, with the $\hat{z}$ axis perpendicular to the remaining crystal face. The $\hat{x} + \hat{y}$ phonon of this crystal was studied.

In order to determine which elastic and photoelastic constants are able to be evaluated, the Brillouin tensors for the material must be known. The following table summarizes the tensors used in this study, and the elastic and photoelastic tensors for LiCAF are also given.

$$\overleftrightarrow{C} = \begin{pmatrix} C_{11} & C_{12} & C_{13} & C_{14} & 0 & 0 \\ C_{12} & C_{11} & C_{13} & -C_{14} & 0 & 0 \\ C_{13} & C_{13} & C_{33} & 0 & 0 & 0 \\ C_{14} & -C_{14} & 0 & C_{44} & 0 & 0 \\ 0 & 0 & 0 & 0 & C_{44} & C_{14} \\ 0 & 0 & 0 & 0 & C_{14} & \frac{1}{2}(C_{11} - C_{12}) \end{pmatrix} \tag{40}$$

$$\overleftrightarrow{p} = \begin{pmatrix} p_{11} & p_{12} & p_{13} & p_{14} & 0 & 0 \\ p_{12} & p_{11} & p_{13} & -p_{14} & 0 & 0 \\ p_{31} & p_{31} & p_{33} & 0 & 0 & 0 \\ p_{41} & -p_{41} & 0 & p_{44} & 0 & 0 \\ 0 & 0 & 0 & 0 & p_{44} & p_{41} \\ 0 & 0 & 0 & 0 & p_{14} & \frac{1}{2}(p_{11} - p_{12}) \end{pmatrix} \tag{41}$$

these are the elasticity and photoelasticity tensors for LiCAF, respectively. Note that there are 6 independent elastic constants and 8 photoelastic constants. From these, the following phonon-direction dependent Brillouin tensors for LiCAF may be generated:

$$\vec{q} = (100):$$

$$\hat{u} = (100) \quad \rho v^2 = C_{11} \qquad\qquad \hat{u} = (010) \quad \rho v^2 = \tfrac{1}{2}(C_{11} - C_{12})$$

$$\overleftrightarrow{T}_{xL} = \epsilon_0^2 \begin{pmatrix} p_{11} & 0 & 0 \\ 0 & p_{12} & \frac{\epsilon_e}{\epsilon_0} p_{41} \\ 0 & \frac{\epsilon_e}{\epsilon_0} p_{41} & \frac{\epsilon_e^2}{\epsilon_0^2} p_{31} \end{pmatrix} \qquad \overleftrightarrow{T}_{xT1} = \epsilon_0^2 \begin{pmatrix} 0 & \tfrac{1}{2}(p_{11} - p_{12}) & \frac{\epsilon_e}{\epsilon_0} p_{41} \\ \tfrac{1}{2}(p_{11} - p_{12}) & 0 & 0 \\ \frac{\epsilon_e}{\epsilon_0} p_{41} & 0 & 0 \end{pmatrix}$$

$$\hat{u} = (001) \quad \rho v^2 = C_{44}$$

$$\overleftrightarrow{T}_{xT2} = \epsilon_0^2 \begin{pmatrix} 0 & \frac{\epsilon_e}{\epsilon_0} p_{41} & \frac{\epsilon_e}{\epsilon_0} p_{44} - \gamma \\ \frac{\epsilon_e}{\epsilon_0} p_{41} & 0 & 0 \\ \frac{\epsilon_e}{\epsilon_0} p_{44} - \gamma & 0 & 0 \end{pmatrix}$$

$$\vec{q} = (010):$$

$$\hat{u} = (010) \quad \rho v^2 = C_{11} \qquad\qquad \hat{u} = (100) \quad \rho v^2 = \tfrac{1}{2}(C_{11} - C_{12})$$

$$\overleftrightarrow{T}_{yL} = \epsilon_0^2 \begin{pmatrix} p_{12} & 0 & 0 \\ 0 & p_{11} & -\frac{\epsilon_e}{\epsilon_0} p_{41} \\ 0 & -\frac{\epsilon_e}{\epsilon_0} p_{41} & \frac{\epsilon_e^2}{\epsilon_0^2} p_{31} \end{pmatrix} \qquad \overleftrightarrow{T}_{yT1} = \epsilon_0^2 \begin{pmatrix} 0 & \tfrac{1}{2}(p_{11} - p_{12}) & \frac{\epsilon_e}{\epsilon_0} p_{41} \\ \tfrac{1}{2}(p_{11} - p_{12}) & 0 & 0 \\ \frac{\epsilon_e}{\epsilon_0} p_{41} & 0 & 0 \end{pmatrix}$$

$$\hat{u} = (001) \quad \rho v^2 = C_{44}$$

$$\overleftrightarrow{T}_{yT2} = \epsilon_0^2 \begin{pmatrix} p_{14} & 0 & 0 \\ 0 & -p_{41} & \frac{\epsilon_e}{\epsilon_0} p_{44} - \gamma \\ 0 & \frac{\epsilon_e}{\epsilon_0} p_{44} - \gamma & 0 \end{pmatrix}$$

$$\vec{q} = (001):$$

$$\hat{u} = (001) \quad \rho v^2 = C_{33} \qquad\qquad \hat{u} = (100) \quad \rho v^2 = C_{44}$$

$$\overleftrightarrow{T}_{zL} = \epsilon_0^2 \begin{pmatrix} p_{13} & 0 & 0 \\ 0 & p_{13} & 0 \\ 0 & 0 & \frac{\epsilon_e^2}{\epsilon_0^2} p_{33} \end{pmatrix} \qquad \overleftrightarrow{T}_{zT1} = \epsilon_0^2 \begin{pmatrix} 0 & p_{14} & \frac{\epsilon_e}{\epsilon_0} p_{44} + \gamma \\ p_{14} & 0 & 0 \\ \frac{\epsilon_e}{\epsilon_0} p_{44} + \gamma & 0 & 0 \end{pmatrix}$$

$$\hat{u} = (0\bar{1}0) \quad \rho v^2 = C_{44}$$

$$\overleftrightarrow{T}_{zT2} = \epsilon_0^2 \begin{pmatrix} p_{14} & 0 & 0 \\ 0 & -p_{41} & \frac{\epsilon_e}{\epsilon_0} p_{44} + \gamma \\ 0 & \frac{\epsilon_e}{\epsilon_0} p_{44} + \gamma & 0 \end{pmatrix}$$

$$\vec{q} = (110)/\sqrt{2}:$$

$$\hat{u} = (110)/\sqrt{2} \quad \rho v^2 = C_{11}$$

$$\overleftrightarrow{T}_{xyL} = \frac{\epsilon_0^2}{2}
\begin{pmatrix}
(p_{11} + p_{12}) & (p_{11} - p_{12}) & \frac{2\epsilon_e}{\epsilon_0} p_{41} \\
(p_{11} - p_{12}) & (p_{11} + p_{12}) & 0 \\
\frac{2\epsilon_e}{\epsilon_0} p_{41} & 0 & \frac{2\epsilon_e^2}{\epsilon_0^2} p_{31}
\end{pmatrix}$$

$$\hat{u} = (1\bar{1}0) \quad \rho v^2 = \tfrac{1}{2}(C_{11} - C_{12})$$

$$\overleftrightarrow{T}_{xyT1} = \frac{\epsilon_0^2}{2}
\begin{pmatrix}
(p_{11} - p_{12}) & 0 & 0 \\
0 & (p_{12} - p_{11}) & \frac{2\epsilon_e^2}{\epsilon_0^2} p_{41} \\
0 & \frac{2\epsilon_e^2}{\epsilon_0^2} p_{41} & 0
\end{pmatrix}$$

$$\hat{u} = (010) \quad \rho v^2 = C_{44}$$

$$\overleftrightarrow{T}_{xyT2} = \frac{\epsilon_0^2}{\sqrt{2}}
\begin{pmatrix}
p_{14} & p_{14} & \frac{\epsilon_e}{\epsilon_0} p_{44} \\
p_{14} & -p_{14} & \frac{\epsilon_e}{\epsilon_0} p_{44} \\
\frac{\epsilon_e}{\epsilon_0} p_{44} & \frac{\epsilon_e}{\epsilon_0} p_{44} & 0
\end{pmatrix}$$

$$\vec{q} = (011)/\sqrt{2}:$$

$$\hat{u} = (011)/\sqrt{2}$$

$$\overleftrightarrow{T}_{yzL} = \frac{\epsilon_0^2}{2}
\begin{pmatrix}
(p_{12} + p_{13} + 2p_{14}) & 0 & 0 \\
0 & (p_{12} + p_{13} - 2p_{14}) & \frac{\epsilon_e^2}{\epsilon_0^2}(2p_{44} - p_{41}) \\
0 & \frac{\epsilon_e^2}{\epsilon_0^2}(2p_{44} - p_{41}) & \frac{\epsilon_e^2}{\epsilon_0^2}(p_{31} - p_{33})
\end{pmatrix}$$

$$\hat{u} = (01\bar{1})/\sqrt{2}$$

$$\overleftrightarrow{T}_{yzT1} = \frac{\epsilon_0^2}{2}
\begin{pmatrix}
(p_{12} - p_{13}) & 0 & 0 \\
0 & (p_{11} - p_{13}) & -\frac{\epsilon_e}{\epsilon_0} p_{41} \\
0 & -\frac{\epsilon_e}{\epsilon_0} p_{41} & \frac{\epsilon_e^2}{\epsilon_0^2}(p_{31} - p_{33})
\end{pmatrix}$$

$$\hat{u} = (100) \quad \rho v^2 = \tfrac{1}{4}(C_{11} - C_{12} + 2C_{14} + 2C_{44})$$

$$\overleftrightarrow{T}_{yzT2} = \frac{\epsilon_0^2}{\sqrt{2}}
\begin{pmatrix}
0 & (p_{14} + \frac{p_{11}}{2} - \frac{p_{12}}{2}) & \frac{\epsilon_e}{\epsilon_0}(p_{41} + p_{44}) \\
(p_{14} + \frac{p_{11}}{2} - \frac{p_{12}}{2}) & 0 & 0 \\
\frac{\epsilon_e}{\epsilon_0}(p_{41} + p_{44}) & 0 & 0
\end{pmatrix}$$

where $\gamma = \frac{\epsilon_e - \epsilon_0}{\epsilon_0^2}$. The $\vec{q}$ terms indicate the direction of the phonon under study, the $\hat{u}$ terms denote the direction of motion of the atoms associated with

the phonon, and the $\overleftrightarrow{T}$ terms are the actual Brillouin tensors for that particular phonon and atomic motion direction.

As stated earlier, we calculate the term $\left[\hat{e}_s \cdot \overleftrightarrow{T^i} \cdot \hat{e}_0 \right]$ to find out which photoelastic constants are seen, with their shifts indicating a method of finding the elastic constants. Without all the algebra, a summary of the terms resulting from the $\left[\hat{e}_s \cdot \overleftrightarrow{T^i} \cdot \hat{e}_0 \right]$ calculations are presented in Table 2. The top row of these tables indicate which phonon (LA, TA1, TA2) is under study, the elastic constant corresponding to that phonon is shown, as is the scattered/incident polarization.

So, by examining the entries in the above set of matrices, providing the samples have the correct orientations, we may observe 5 of the 6 elastic constants (all except for C_{13}) and all 8 photoelastic constants. To summarize, Table 3 gives the scattering geometry required to see each of the different elastic and photoelastic constants.

Unfortunately, due to sample unavailability, we were unable to study the $\hat{y} + \hat{z}$ crystalline orientation; therefore the C_{14} elastic constant was unable to be observed. This limits us to seeing four of the six elastic constants, and possibly all of the photoelastic constants. The Brillouin data used in this analysis is given in Figures 9-12. In each figure, the data is presented with the Quartz data on top in a small window, with the corresponding LiCAF data given directly below.

Photoelastic and Elastic Constant Analysis

As is immediately obvious from the data, the $\hat{x} + \hat{y}$ phonon with $H_S V_0$ polarization resulted in no data, and thus the two photoelastic constants p_{41} and p_{44} must both be too small to be detected with our experimental arrangement.

The analysis begins with examining the $\left[\hat{e}_s \cdot \overleftrightarrow{T^i} \cdot \hat{e}_0 \right]$ elements possessed by Quartz. Given that Quartz is an isotropic material:

$$\hat{q} = (010)$$

	[L]	[T_1]	[T_2]
$\rho v^2 =:$	C_{11}	$(C_{11} - C_{12})/2$	C_{44}
$V_S V_0$	$\epsilon_0^2 p_{12}$	0	$\epsilon_0^2 p_{14}$
$V_S H_0$	0	$\dfrac{\frac{c_0^2}{2}(p_{11}-p_{12})-\epsilon_e\epsilon_0 p_{41}}{\sqrt{2}}$	0
$H_S H_0$	$\dfrac{c_0^2 p_{11}-c_e^2 p_{31}}{2}$	0	$\dfrac{-c_0^2 p_{14}}{2}$
$H_S V_0$	0	$\dfrac{\frac{c_0^2}{2}(p_{11}-p_{12})+\epsilon_e\epsilon_0 p_{41}}{\sqrt{2}}$	0

$$\hat{q} = (001)$$

	[L]	[T_1]	[T_2]
$\rho v^2 =:$	C_{33}	C_{44}	C_{44}
$V_S V_0$	$\epsilon_0^2 p_{13}$	0	$\epsilon_0^2 p_{14}$
$V_S H_0$	0	$\dfrac{c_0^2 p_{14}+\epsilon_e\epsilon_0 p_{44}+\gamma}{\sqrt{2}}$	0
$H_S H_0$	$\dfrac{c_e^2 p_{33}-c_0^2 p_{13}}{2}$	0	$\dfrac{c_0^2 p_{14}}{2}$
$H_S V_0$	0	$\dfrac{-c_0^2 p_{14}+\epsilon_e\epsilon_0 p_{44}+\gamma}{\sqrt{2}}$	0

$$\hat{q} = (110)/\sqrt{2}$$

	[L]	[T_1]	[T_2]
$\rho v^2 =:$	C_{11}	$(C_{11} - C_{12})/2$	C_{44}
$V_S V_0$	$\epsilon_0^2 p_{31}$	0	0
$V_S H_0$	0	$-\epsilon_e\epsilon_0 p_{41}$	$\dfrac{\epsilon_e\epsilon_0 p_{44}}{\sqrt{2}}$
$H_S H_0$	$\frac{c_0^2}{2}(p_{11} - p_{12})$	0	$\dfrac{c_0^2 p_{14}}{\sqrt{2}}$
$H_S V_0$	$-\epsilon_e\epsilon_0 p_{41}$	0	$\dfrac{-\epsilon_e\epsilon_0 p_{44}}{\sqrt{2}}$

$$\hat{q} = (011)/\sqrt{2}$$

	[L]	[T_1]	[T_2]
$\rho v^2 =:$			$(C_{11} - C_{12} + 2C_{14} + 2C_{44})/4$
$V_S V_0$	$\frac{c_0^2}{2}(p_{11} + p_{31} + 2p_{14})$	$\frac{c_0^2}{2}(p_{12} - p_{13})$	0
$V_S H_0$	0	0	$\frac{c_0^2}{\sqrt{2}}\left(\frac{p_{11}}{2} - \frac{p_{12}}{2} + p_{14}\right)$
$H_S H_0$	$\frac{\epsilon_e\epsilon_0}{2}(2p_{44} - p_{41})$	$\dfrac{-\epsilon_e\epsilon_0 p_{41}}{2}$	0
$H_S V_0$	0	0	$\frac{\epsilon_e\epsilon_0}{\sqrt{2}}(p_{44} + p_{41})$

Table II. Terms relating photoelastic constants seen in LiCAF to phonon and polarization.

Constant(s)	Phonon	Polarization
p_{12}	$\hat{y}$	$V_S V_0$
p_{11}	$\hat{y}$	$H_S H_O$
p_{13}	$\hat{z}$	$V_S V_0$
p_{33}	$\hat{z}$	$H_S H_O$
p_{31}	$\hat{x} + \hat{y}$	$V_S V_0$
p_{41}, p_{44}	$\hat{x} + \hat{y}$	$H_S V_0$
p_{14}	$\hat{x} + \hat{y}$	$H_S H_0$
C_{12}	$\hat{y}$	$H_S V_0$
C_{33}	$\hat{z}$	$V_S V_0$
C_{11}	$\hat{x} + \hat{y}$	$V_S V_0$
C_{44}	$\hat{x} + \hat{y}$	$H_S H_0$
C_{14}	$\hat{y} + \hat{z}$	$H_S V_0$

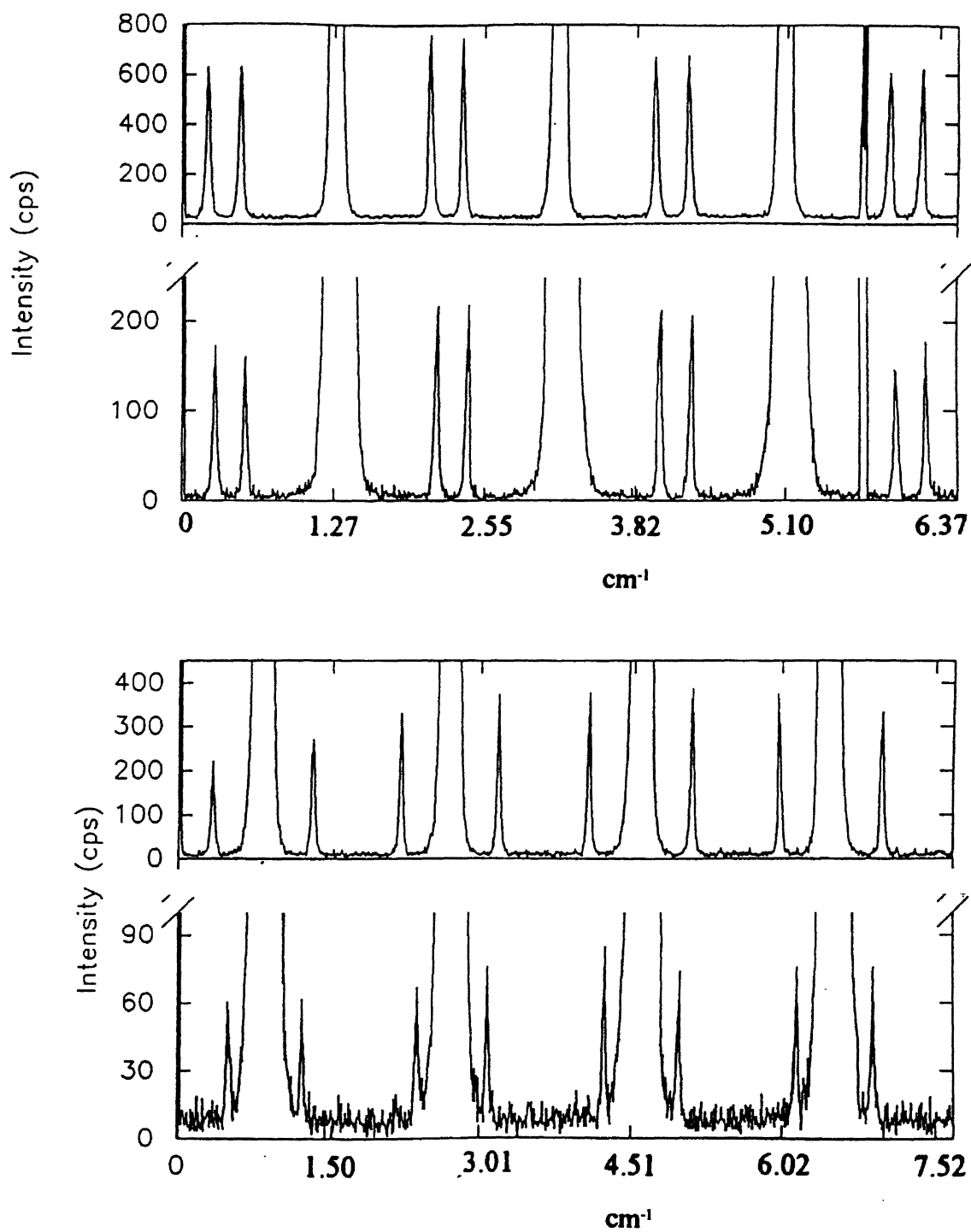Table III. Photoelastic constants seen in LiCAF.

Figure 9. Brillouin data for Undoped LiCAF: Y phonon, VsVo (top); and Y phonon, HsVo (bottom).
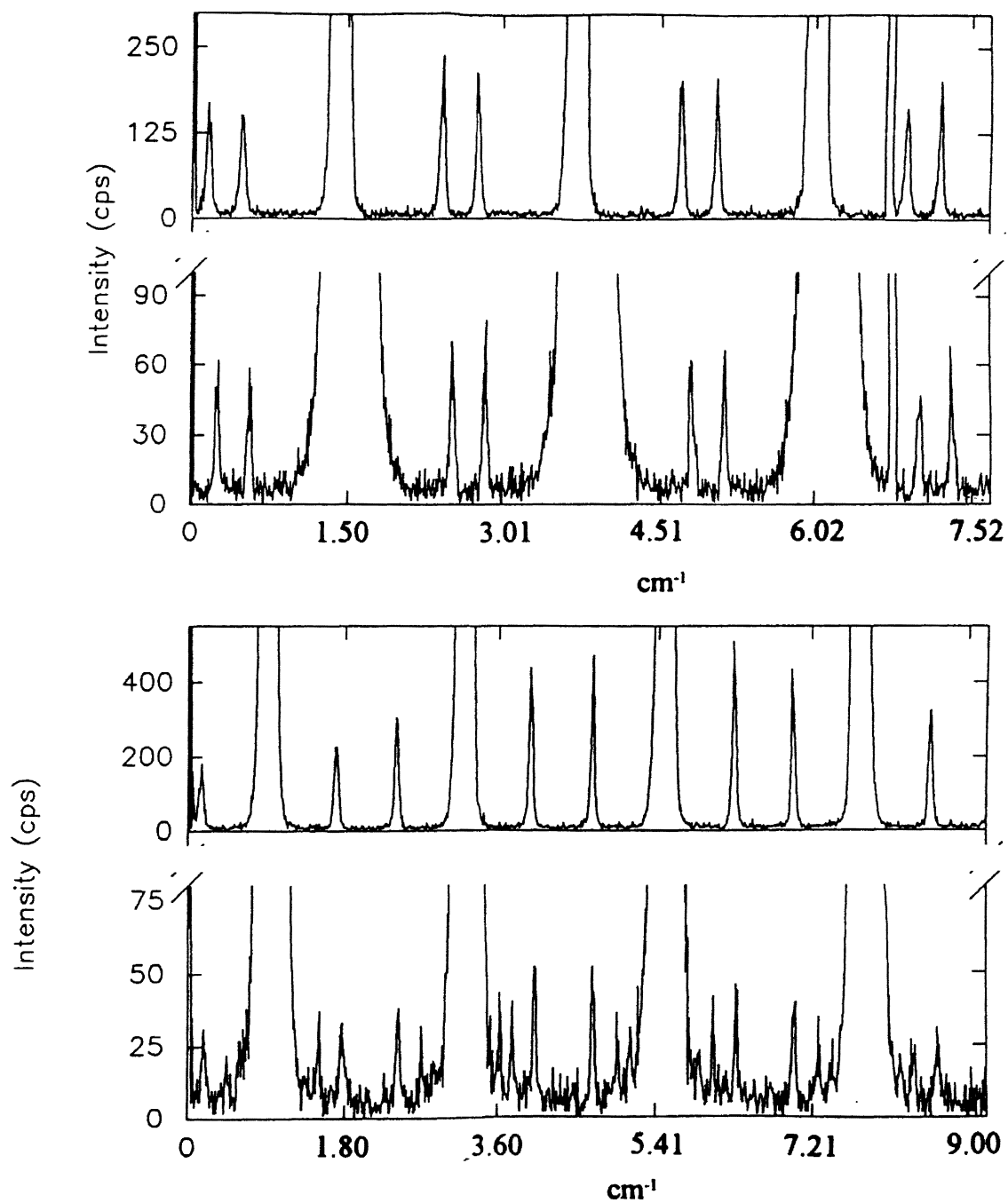
Figure 10. Brillouin data for Undoped LiCAF: Y phonon, HsHo (top); and X+Y phonon, HsHo (bottom).
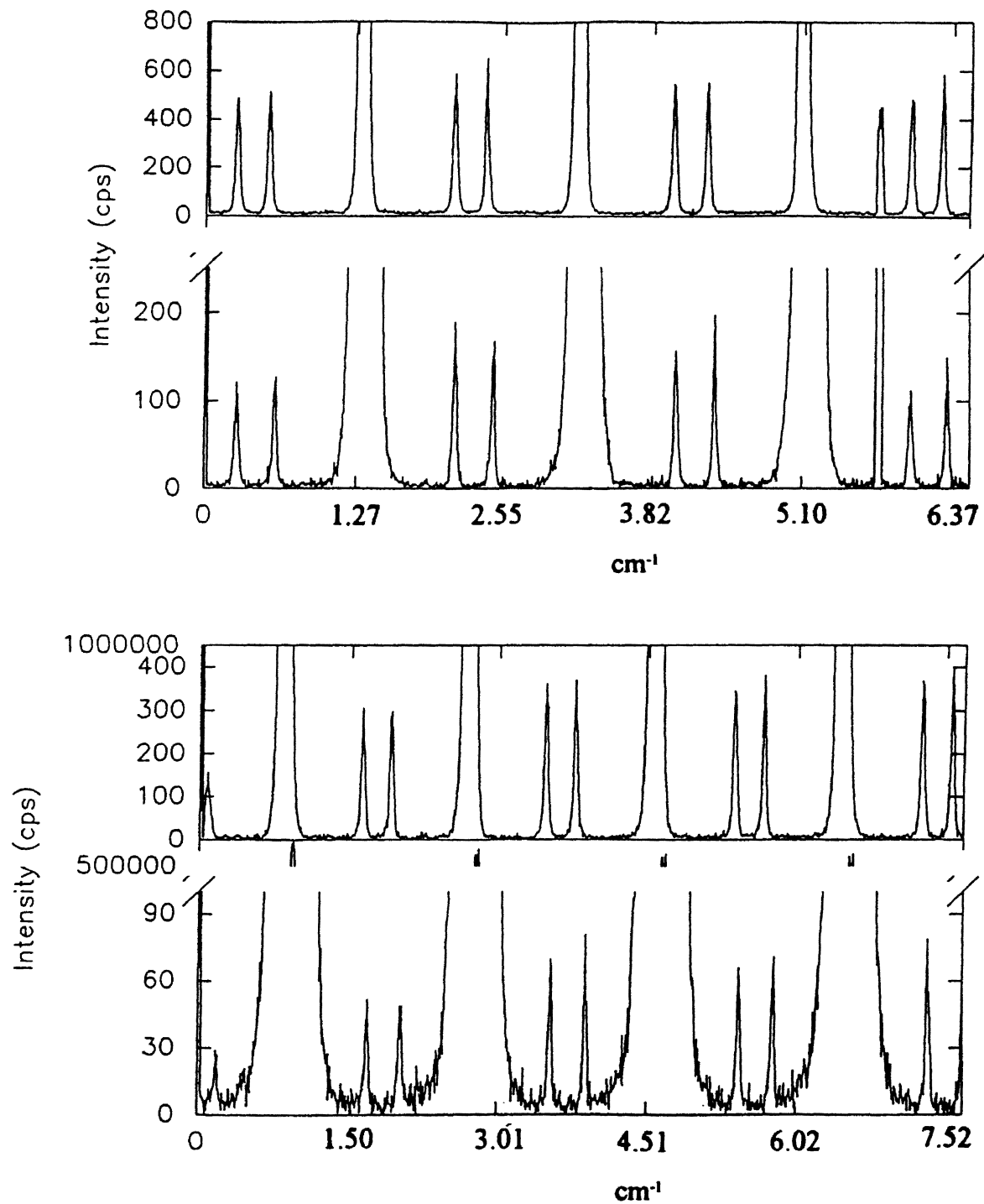
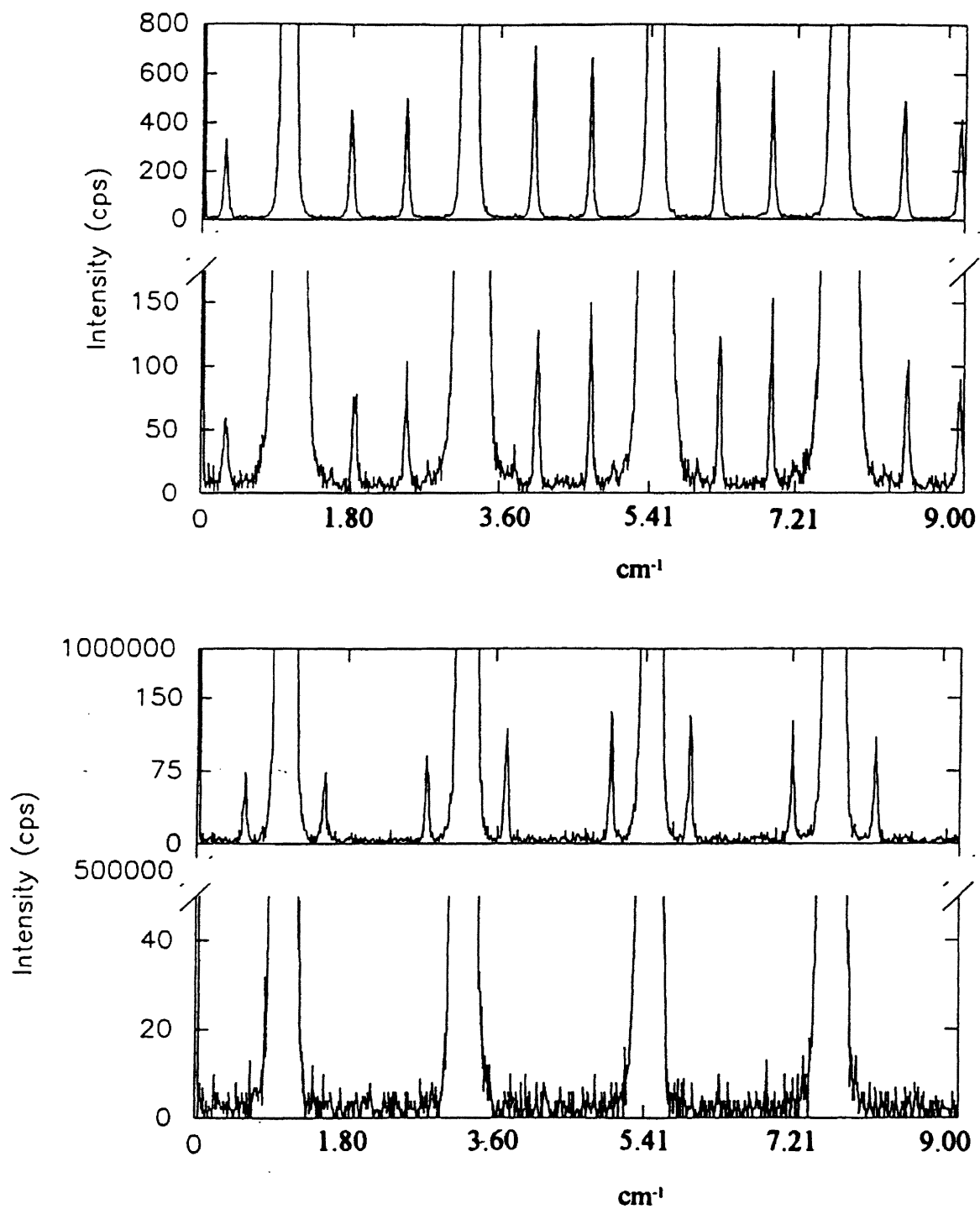Figure 11. Brillouin data for Undoped LiCAF: Z phonon, VsVo (top); and Z phonon, HsHo (bottom).

Figure 12. Brillouin data for Undoped LiCAF: X+Y phonon, VsVo (top); and X+Y phonon, HsVo (bottom).

$$\hat{q} = (100)$$

	$[L]$	$[T_1]$	$[T_2]$
$V_S V_0$	$\epsilon_0^2 p_{12}$	0	0
$V_S H_0$	0	0	$\frac{\epsilon_0^2 p_{44}}{\sqrt{2}}$
$H_S V_0$	0	0	$\frac{\epsilon_0^2 p_{44}}{\sqrt{2}}$
$H_S H_0$	$\epsilon_0^2 p_{44}$	0	0

with $p_{44} = \frac{(p_{11} - p_{12})}{2}$. These are the $\left[\hat{e}_s \cdot \overleftrightarrow{T^i} \cdot \hat{e}_0 \right]_{std}$ values to be used in 39.

Reference values for Quartz used in this study are: $p_{12} = 0.279$ and $p_{44} = 0.0787$, with $(\Delta\omega_{Br})_{LA} = 0.801 cm^{-1}$ and $(\Delta\omega_{Br})_{TA} = 0.504 cm^{-1}$.

All of the data generated for this study is summarized in Table 4. This data was used in the computation of the elastic and photoelastic constants, and an example calculation of each is now presented. Examining the data values generated in the L-XY-VV orientation, we find:

$$\left[\hat{e}_s \cdot \overleftrightarrow{T^i} \cdot \hat{e}_0 \right]_{L-XY-VV} = (\epsilon_0^2 p_{31})_{LiCAF}$$

$$\left[\hat{e}_s \cdot \overleftrightarrow{T^i} \cdot \hat{e}_0 \right]_{Quartz} = (\epsilon_0^2 p_{12})_{Quartz}$$

therefore:

$$(\epsilon_0^2 p_{31})_{LiCAF} = \left(\frac{2.95}{2.205} \right)^{\frac{1}{2}} (0.17307)^{\frac{1}{2}} \left[\frac{(2.3934)}{(2.462)} \right]^2 \left(\frac{1.462}{1.3934} \right) \left(\frac{0.8248}{0.801} \right) (\epsilon_0^2 p_{12})_{Quartz}$$

or:

$$(\epsilon_0^2 p_{31})_{LiCAF} = 0.1668$$

The elastic constant is determined from the Brillouin shift and the phonon velocity:

$$\rho v_{LiCAF}^2 = C_{11} = \rho \left(\frac{\lambda_0 c \Delta\omega_{Br}}{2n \sin\left(\frac{\theta}{2}\right)} \right)^2$$

so:

$$C_{11} = 2.95 \left[\frac{(3x10^{10})(514.5x10^{-7})(0.8248)}{2(1.3934)\sin(\frac{\pi}{4})} \right]^2 \text{ Dynes/cm}^2$$

FILENAME	INTEGRATED INTENSITY RATIO (I_{LiCAF}/I_{Quartz})	BRILLOUIN SHIFT (cm^{-1})
L-Y-VV	0.54599	0.8125
L-Y-HV	0.15023	0.3655
L-Z-VV	0.24164	0.7708
L-Z-HH	0.16130	0.7675
L-XY-VV	0.17307	0.8248
L-XY-HH	0.09619 (LA)	0.8064
	0.04373 (TA)	0.5526
L-XY-HV	not detected	not detected

Table IV. Brillouin Data Generated for LiCAF.

or:

$$C_{11} = 1.230x10^{12} \text{ Dynes/cm}^2$$

Table 5 summarizes the results of evaluating expression 39 for each photoelastic constant expression and using the correct expression (31, 32, or 33) for the elastic constants.

Thus our analysis has obtained numerical values for 7 of the 8 photoelastic constants, and 4 of the 6 Elastic constants. Additional samples may have been able to shed more light upon our analysis.

Photoelastic Constant	Expt. value	Std. Dev. $(\times 10^{-2})$	Elastic Constant	velocity $(\times 10^5$ cm/sec$)$	Expt. value $(\times 10^{12}$ Dyn/cm$^2)$
p_{11}	0.358 ± 0.0037	1.070			
p_{12}	0.290 ± 0.024	2.767	C_{11}	6.384	1.202
p_{13}	0.183 ± 0.0066	1.763	C_{12}	2.863	0.719
p_{14}	0.036 ± 0.0026	1.070	C_{33}	6.025	1.071
p_{31}	0.167 ± 0.0050	1.062	C_{44}	4.328	0.553
p_{33}	0.268 ± 0.0091	3.656			
p_{41}	-0.0034 ± 0.0017	1.660			

Table V. LiCAF Photoelastic and Elastic constant values.

BIBLIOGRAPHY

1. DeYoreo, J., OSU Colloquium Presentation, Fall 1991, Lawrence Livermore National Labs.

2. Payne, S., Chase, L., Unpublished Results, Lawrence Livermore National Labs.

3. Payne, S., Chase, L., Newkirk, H., Smith, L., and Krupke, W., $LiCaAlF_6$: A Promising New Solid State Laser Material, IEEE Journal of Quantum Electronics, Vol. 24, 11, 1988.

4. Payne, S., Chase, L., Atherton, L., Caird, J., Kway, W., Shinn, M., Hughes, R., and Smith, L., Properties and performance of the $LiCaAlF_6:Cr^{3+}$ laser material, SPIE, Solid State Lasers, Vol. 1223, 1990.

5. Colthup, N.B., Daly, L.H., Wiberley, S.E., Introduction to Infrared and Raman Spectroscopy, Academic Press, Inc., New York, 1975.

6. Wicksted, J.P., Unpublished Letter to L. Chase, 1990.

7. Porto, S.P.S., Light Scattering With Laser Sources, International Conference on Light Scattering in Solids, Wright, G.B. (ed), Springer-Verlag, New York, 1969.

8. Hayes, W., Loudon, R., Scattering of Light by Crystals, Wiley-Interscience, New York, 1978.

9. Steele, D., Theory of Vibrational Spectroscopy, W. B. Saunders and Co., Philadelphia, 1971.

10. Tolbin, M.C., Laser Raman Spectroscopy, Wiley-Interscience, New York, 1971.

11. Cherlow, J.M., Porto, S.P.S., Laser Raman Spectroscopy of Gases, Walther, H. ed, Topics in Applied Physics, vol 2, Laser Spectroscopy of Atoms and Molecules, Springer-Verlag, Berlin, 1976.

12. Chu, B., Laser Light Scattering, Academic Press, Inc., New York, 1974.

13. Kittel, C., Introduction to Solid State Physics (6th ed.), John Wiley and Sons, Inc., New York, 1986.

14. Cummins, H.Z., Shoen, P.E., Linear Scattering from Thermal Fluctuations, Arecchi and Shultz-DuBois (eds.), Laser Handbook, vol. 2, North-Holland Publishing Co., Amsterdam, 1972.

15. Nye, J.F., Physical Properties of Crystals, Clarendon Press, Oxford, 1981.

16. International Tables of X-ray Crystallography, International Union of Crystallography, Kynoch Press, Birmingham, England, 1952.

VITA

CHARLES E. HASTY

Candidate for the Degree of

Master of Science

Thesis: RAMAN AND BRILLOUIN SCATTERING IN LiCAF AND LiSAF
CRYSTALS

Major Field: Physics

Biographical:

Personal Data: Born in Ponca City, Oklahoma, January 28, 1968, the son of
Wallace and Margaret Hasty.

Education: Received Bachelor of Science Degree in Physics from Oklahoma
State University, Stillwater, Oklahoma, 1990; completed requirements
for the Master of Science Degree in Physics at Oklahoma State Univer-
sity, Stillwater, Oklahoma in December, 1993.